

Dynamic Subgrid Turbulence Modeling for Shallow Cumulus Convection Simulations beyond LES Resolutions

GEORGIOS A. EFSTATHIOU ^a

^a *Department of Mathematics and Statistics, University of Exeter, Exeter, United Kingdom*

(Manuscript received 7 June 2022, in final form 10 February 2023, accepted 13 March 2023)

ABSTRACT: A scale-dependent dynamic Smagorinsky model is implemented in the Met Office/NERC Cloud (MONC) model using two averaging flavors, along Lagrangian pathlines and local moving averages. The dynamic approaches were compared against the conventional Smagorinsky–Lilly scheme in simulating the diurnal cycle of shallow cumulus convection. The simulations spanned from the LES to the near-gray-zone and gray-zone resolutions and revealed the adaptability of the dynamic model across the scales and different stability regimes. The dynamic model can produce a scale- and stability-dependent profile of the subfilter turbulence length scale across the chosen resolution range. At gray-zone resolutions the adaptive length scales can better represent the early precloud boundary layer leading to temperature and moisture profiles closer to the LES compared to the standard Smagorinsky. As a result, the initialization and general representation of the cloud field in the dynamic model is in good agreement with the LES. In contrast, the standard Smagorinsky produces a less well-mixed boundary layer, which fails to ventilate moisture from the boundary layer, resulting in the delayed spinup of the cloud layer. Moreover, strong downgradient diffusion controls the turbulent transport of scalars in the cloud layer. However, the dynamic approaches rely on the resolved field to account for nonlocal transports, leading to overenergetic structures when the boundary layer is fully developed and the Lagrangian model is used. Introducing the local averaging version of the model or adopting a new Lagrangian time scale provides stronger dissipation without significantly affecting model behavior.

KEYWORDS: Turbulence; Boundary layer; Subgrid-scale processes


1. Introduction

Atmospheric modeling has come a long way since the early use of quasigeostrophic models to capture the synoptic-scale atmospheric dynamics, as first attempted in the mid-twentieth century (Charney et al. 1950; Bolin 1955). Nowadays, numerical weather prediction (NWP) models solve the full set of Navier–Stokes and other prognostic conservation equations on high-resolution grids, exhibiting significantly increased forecasting skill since NWP first became operational. This steady but substantial improvement in our ability to predict the future state of the atmosphere has led to more accurate weather forecasts, especially those related to severe weather events with serious socioeconomic impact (Bauer et al. 2015).

Two modeling frameworks can be identified related to the relative size and properties of the applied filter (Δ) on the Navier–Stokes equations: the Reynolds-averaged Navier–Stokes (RANS) and the large-eddy simulation (LES) models (Pope 2000; Honnert et al. 2020). In RANS, which has been the cornerstone of NWP development, the filter scale needs to be much larger than the dominant scales of turbulence, in order to justify the filter expressing an *ensemble average* over a number of different flow realizations. A clear separation of scales is assumed between the ensemble-averaged subgrid fluxes

and the resolved mean flow. On the other end, the LES equations are spatially filtered with Δ representing a spatial (three-dimensional) filter that needs to clearly resolve the inertial subrange of turbulent motions. Therefore, an LES subfilter turbulence scheme should represent the continuous transfer of energy from the production to the dissipation scales under a local equilibrium. One should note here that the term subgrid is not the same as subfilter, with the latter representing scales below the “effective resolution” of the model, which is controlled by the combined impact of the numerical discretization, the grid size, and imposed physical diffusion. Throughout the rest of the paper the term subgrid will be used to refer to the unresolved motions.

Wyngaard (2004) first identified a new emerging regime of simulations where the dominant scales of turbulent motion are comparable to the grid spacing. He named this resolution regime the “terra incognita,” i.e., an uncharted territory or a “gray zone” where neither RANS nor LES subgrid parameterizations are appropriate. The fundamental assumptions behind both modeling approaches are violated as there is no clear separation between the production and dissipation scales of turbulence in the boundary layer (BL). Nonetheless, the increased computational power available and the need for more localized forecasts has led weather centers around the world to push the horizontal resolution of their NWP models to the subkilometric scales (e.g., Boule et al. 2016).

 Denotes content that is immediately available upon publication as open access.

Corresponding author: Georgios Efstathiou, g.efstathiou@exeter.ac.uk



This article is licensed under a [Creative Commons Attribution 4.0 license](http://creativecommons.org/licenses/by/4.0/) (<http://creativecommons.org/licenses/by/4.0/>).

DOI: 10.1175/JAS-D-22-0132.1

© 2023 American Meteorological Society. For information regarding reuse of this content and general copyright information, consult the [AMS Copyright Policy](http://www.ametsoc.org/PUBSReuseLicenses) (www.ametsoc.org/PUBSReuseLicenses)

At the same time, even though recent research has shown some improvements in the simulation of heavy rainfall events with increasing horizontal resolution (Warren et al. 2014), it has also revealed significant challenges as this improvement is not as pronounced as expected (Ito et al. 2017) and is very sensitive to the treatment of the unresolved turbulence length scales (Beare 2014; Hanley et al. 2015; Verrelle et al. 2015). Therefore, the gray zone might be stalling the further development and improvement of NWP (Ito et al. 2017; Honnert et al. 2020).

Moreover, Wyngaard (2004) proposed solving the prognostic subfilter turbulent transport equations to account for the transition of turbulent transfer from the LES to the fully parameterized limit. Considering an algebraic form of the equations, eddy diffusivity becomes a tensor that can model flow changes from isotropic small-scale turbulence at the LES limit to more anisotropic flow in the gray zone and at mesoscale resolutions. However, solving a full set of conservation equations would be computationally expensive while requiring suitable closure assumptions between the LES and RANS regimes. Juliano et al. (2022) introduced a three-dimensional (3D) version of the Mellor–Yamada BL scheme for gray-zone simulations, acknowledging the need to improve the turbulent-length-scale formulation (see the work of Ito et al. 2015).

Instead, a growing number of new gray-zone parameterizations are being developed, largely based on extending existing LES or RANS schemes. Shin and Hong (2015) modified a non-local K -profile model to reduce the parameterized transport in the gray zone with Lancz et al. (2018) following a similar approach for a mass-flux scheme. Boutle et al. (2014) blended a 3D LES and a 1D RANS scheme to successfully simulate a stratocumulus deck using the Met Office operational Unified Model. From a coarse LES perspective, Efstathiou and Beare (2015) explored and modified an LES turbulence closure to quantify the transition of turbulent fluxes in the BL gray zone. Zhang et al. (2018) blended the turbulence length scales from the LES to the RANS limit while Kurowski and Teixeira (2018) and Zhou et al. (2021) merged between the two asymptotic length-scale limits (LES and RANS) to make a 3D turbulence kinetic energy (TKE) scheme adaptive to gray-zone resolutions. For an in-depth review of the gray-zone literature, see Honnert et al. (2020).

At gray-zone resolutions turbulent motions become partially resolved depending on the relative size of the dominant turbulence length scales (Λ) compared to the grid spacing as expressed by the similarity relationship Λ/Δ (Honnert et al. 2011). Furthermore, the turbulence length scales evolve with BL or cloud development and as a result Λ/Δ changes in time and space. Hence, a simulation may be passing from different resolution regimes (from the gray zone to the near-gray zone and LES), at different parts of the flow (near surface, mixed layer, inversion, cloud layer) regardless of the initial grid length choice [see Fig. 6 of Honnert et al. (2020) for a schematic representation]. Taking also into account the increased sensitivity of the resolved TKE to the subgrid mixing (Beare 2014), as manifested by the impact of the subgrid mixing length scales on cloud morphology (Hanley et al. 2015; Verrelle et al. 2015), it

becomes evident that specifying a single universal subgrid mixing parameter is at least problematic, especially in the gray zone.

Dynamic turbulence modeling was introduced by Germano et al. (1991) in an attempt to avoid the a priori specification of closure parameters in LES turbulence models. It is based on an algebraic identity that relates the smallest resolvable motions to the subgrid stresses, expressing a form of scale similarity between the unresolved and the smallest resolved turbulent eddies. They used the Smagorinsky eddy-diffusivity scheme (Smagorinsky 1963; Lilly 1967) to dynamically derive the tunable Smagorinsky coefficient (C_S) that controls the subgrid mixing length and in turn the rate of transfer from the dominant to the dissipation scales. Furthermore, due to the local variability of C_S , it became apparent that some form of averaging is usually required (Lilly 1992). Porté-Agel et al. (2000) extended the dynamic Smagorinsky to make C_S scale dependent, resulting in an increased adaptivity at different flow regimes. Even though a converging LES should rely much less on the choice of the subgrid scheme (Pope 2000), in practice, setting an appropriate Δ to represent the inertial subrange of turbulence for a variety of flows is not always computationally feasible. For example, near the surface the solid boundary confines turbulence length scales resulting in underresolved turbulence and no clear separation of scales. The conventional Smagorinsky becomes overdissipative in this regime failing to reproduce the surface-layer scaling arguments, while, in contrast, the scale-dependent dynamic Smagorinsky is able to better capture the log law and corresponding momentum transfer (see Porté-Agel et al. 2000; Kirkil et al. 2012).

Based on the improved behavior of the dynamic Smagorinsky where turbulence is only partially resolved, Efstathiou et al. (2018) modified and extended the Lagrangian-averaged scale-dependent dynamic model of Bou-Zeid et al. (2005) to the atmospheric BL gray zone. The dynamic approach was able to better reproduce mean profiles and turbulence statistics in an evolving BL compared to the standard Smagorinsky across a range of near-gray-zone resolutions. Coarse simulations remained relatively invariant to resolution changes due to the strong scale dependence exhibited by the dynamic model. This scale dependence of the C_S is paramount in better representing the BL at gray-zone resolutions since it “relaxes” the assumption of Δ lying in the inertial subrange (Porté-Agel et al. 2000). However, the dynamic approach can reach its usability limit when the grid becomes too coarse to resolve any turbulent structures, as the scheme relies on sampling from the smallest resolvable scales.

Even though there have been very limited applications of dynamic schemes in moist convection case studies, these have shown promising results especially compared to conventional approaches. Kirkpatrick et al. (2006) used a scale-invariant dynamic Smagorinsky at LES resolutions, which performed significantly better compared to the conventional Smagorinsky, giving the closest agreement with observations in simulating a stratocumulus case. Simulating the same case study, Shi et al. (2018) found a more accurate representation of turbulent transfer and BL properties

across a wide range of resolutions when using dynamic models and especially the dynamic reconstruction model (Chow et al. 2005). In addition, Shi et al. (2019) utilized the same turbulence closure to achieve better agreement between LES and kilometeric deep convection simulations, mainly due to its ability to produce countergradient fluxes.

In this study, we implement the Lagrangian-averaged scale-dependent dynamic Smagorinsky (LASD) model in the newly developed Met Office/NERC Cloud (MONC) model, to examine its ability to reproduce the well-studied Atmospheric Radiation Measurement (ARM) shallow cumuli convection case (Brown et al. 2002) against the conventional Smagorinsky model from the LES to the gray zone. We also introduce a locally averaged version of the scheme as a more practical implementation of LASD and test a new formulation for the Lagrangian time scale in the original scheme. The C_S averaging can be regarded as a pragmatic choice based on a suitable compromise between local length-scale smoothness to keep the scheme numerically stable while still capturing its spatio-temporal variations. Therefore, investigating the effects of the averaging procedures can provide further insight on the dynamic model behavior.

Nonetheless, the comparison between the static and dynamic approaches can reveal some substantial shortcomings in the representation of turbulence in the BL and cloud layer when using a conventional Smagorinsky closure (Petch et al. 2002). Here, we revisit the ARM case and apply for the first time a dynamic Smagorinsky scheme in a shallow cumuli case to examine the impact of dynamically deriving the subgrid mixing length scales on BL development and cloud representation beyond the LES limit.

2. Model description (MONC)

MONC is a highly scalable, 3D LES/cloud-resolving model (Brown et al. 2015). The scientific basis for MONC is the Met Office Large Eddy Model (LEM), which has been used extensively to study the BL gray zone (e.g., Beare 2014; Efstathiou and Beare 2015; Efstathiou et al. 2016; Efstathiou and Plant 2019). The filtered 3D Navier–Stokes equations are solved in an anelastic form using a centered-difference advection scheme (Piacsek and Williams 1970) for the momentum components and a total variation diminishing scheme (Leonard et al. 1993) for the perturbation potential temperature and total water equation. In the anelastic approximation a hydrostatic reference state is defined for temperature, pressure and density (ρ_0), which is a function of height (z) only. The model uses an all-or-nothing saturation scheme, with liquid water mixing ratio (q_l) set diagnostically to $q_l = \max(0, q_t - q_{\text{sat}})$, where q_{sat} is the saturation mixing ratio and q_t is the total water mixing ratio, expressed as the sum of water vapor (q_v) and liquid water mixing ratio ($q_l = q_v + q_l$).

Subfilter turbulence modeling

In LES, a low-pass filter partitions the flow into subfilter and resolved-scale motions. Subfilter fluxes require modeling to ensure the proper representation of the energy cascade to

avoid any unrealistic buildup of energy at the grid scale. The subfilter momentum stress tensor (τ_{ij}) is given by

$$\tau_{ij} = \rho_0(\overline{u_i u_j} - \overline{u_i} \overline{u_j}), \quad (1)$$

where the overbar denotes the LES filter. As the nature of the spatial LES filtering does not satisfy the Reynolds averaging rules, scale interactions produce extra contributions to the stress tensor (Leonard 1975). Since the turbulence models described below do not explicitly account for the extra stresses included in Eq. (1), we are treating the overbar as the grid-scale filter and any motions smaller as subgrid-scale (SGS) motions for simplicity.

Similarly, for the SGS heat flux ($\tau_{\theta j}$),

$$\tau_{\theta j} = \rho_0(\overline{u_j \theta} - \overline{u_j} \overline{\theta}), \quad (2)$$

where θ is the potential temperature. The rest of the scalar variables (water vapor and liquid water) SGS fluxes are represented by

$$\tau_{q,j} = \rho_0(\overline{u_j q_r} - \overline{u_j} \overline{q_r}), \quad (3)$$

with q_r corresponding to the different water species such as q_v for water vapor and q_l for liquid water, respectively.

1) THE SMAGORINSKY SCHEME

The Smagorinsky scheme (Smagorinsky 1963) aims to reproduce the cascade of energy from the production to the dissipation scales by introducing the Smagorinsky coefficient (C_S) that is derived assuming a constant rate of energy transfer in the inertial subrange. The stress tensor is modeled with an eddy-viscosity approach that relates (the deviatoric part of) the stress to the (shear) strain rate tensor (S_{ij}):

$$\tau_{ij} = -2\rho_0\nu_T\overline{S_{ij}}f_m(\text{Ri}), \quad (4)$$

with

$$\overline{S_{ij}} = \frac{1}{2}\left(\frac{\partial\overline{u_i}}{\partial x_j} + \frac{\partial\overline{u_j}}{\partial x_i}\right). \quad (5)$$

The overbar denotes resolved quantities: i.e., filtered at the scale Δ . The eddy viscosity (ν_T) is given by

$$\nu_T = \lambda^2|\overline{S}|, \quad (6)$$

where $|\overline{S}| = (2\overline{S_{ij}}\overline{S_{ij}})^{1/2}$ is the modulus of the strain rate tensor and λ is the SGS mixing length,

$$\lambda = C_S\Delta. \quad (7)$$

Stratification effects on λ are taken into account through the use of $f_m(\text{Ri})$, which is the stability function for momentum as a function of the Richardson number (Ri) and described in the appendix.

To control the excessively dissipative nature of the Smagorinsky scheme close to the ground, a wall-damping function was proposed by Mason and Thomson (1992) for λ :

$$\frac{1}{\lambda^2} = \frac{1}{(\kappa z)^2} + \frac{1}{(C_S \Delta)^2}. \quad (8)$$

The default MONC configuration uses $C_S = 0.23$ and $\Delta = \Delta x$, with Δx expressing the horizontal grid spacing and κ the von Kármán constant set to 0.4. Similarly, for the SGS heat flux we have

$$\tau_{\theta j} = -\rho_0 \frac{\nu_T}{\text{Pr}} \frac{\partial \bar{\theta}}{\partial x_j} f_h(\text{Ri}), \quad (9)$$

where Pr is the SGS Prandtl number equal to 0.7 and $f_h(\text{Ri})$ is the stability function for heat. For the SGS water species flux,

$$\tau_{q,j} = -\rho_0 \frac{\nu_T \bar{q}_r}{\text{Pr}} \frac{\partial}{\partial x_j} f_h(\text{Ri}). \quad (10)$$

2) THE SCALE-DEPENDENT DYNAMIC SMAGORINSKY MODEL

The dynamic model utilizes the smallest resolved scales of turbulence to calculate a flow-appropriate C_S value. The dynamic approach is based on the Germano identity (Germano et al. 1991), which relates the stresses at two different scales with the fluxes at their intermediate scales:

$$L_{ij} = T_{ij} - \tilde{\tau}_{ij} = \widetilde{\bar{u}_i \bar{u}_j} - \tilde{u}_i \tilde{u}_j, \quad (11)$$

where the tilde denotes test filtering at the scale of $\alpha\Delta$ ($\alpha > 1$), T_{ij} is the SGS stress tensor at $\alpha\Delta$, and L_{ij} is the resolved stress tensor associated with eddies with length scales intermediate between Δ and $\alpha\Delta$. Note that ρ_0 has been removed from all terms in Eq. (11) as a constant factor.

The Germano identity can be used with any SGS stress tensor model. Originally, Germano et al. (1991) applied the dynamic procedure in the Smagorinsky scheme to alleviate the need for a priori specifying C_S . The adaptivity of the length scales [through Eq. (7)] makes the dynamic Smagorinsky attractive for use in gray-zone resolutions. However, even the dynamically estimated C_S implies the presence of a clear inertial subrange of turbulence as C_S remains scale invariant [$C_{S(\alpha\Delta)} = C_{S(\alpha^2\Delta)}$]. Therefore, scale dependency [$C_{S(\alpha\Delta)} \neq C_{S(\alpha^2\Delta)}$] is paramount in the representation of SGS turbulence length scales in the gray zone where $\Delta \sim \Lambda$ and the scale-invariance assumption is no longer valid because the test filter scale does not lie within the inertial subrange. The scale-dependent procedure (see Porté-Agel et al. 2000) is based on applying the Smagorinsky model at the grid-filter scale (Δ) and at two different test filter scales ($\alpha\Delta$ and $\alpha^2\Delta$).

Here we implement in MONC the LASD model of Bou-Zeid et al. (2005), following the work of Efstathiou et al. (2018), which also incorporates the stability functions (see appendix) as a self-consistent aspect of the dynamic procedure (see also Kirkpatrick et al. 2006). Applying the Smagorinsky model [Eqs. (6), (7), and (4)] at the first test filter scale ($\alpha = 2$) results in

$$T_{ij} = -2C_{S(2\Delta)}^2 (2\Delta)^2 |\tilde{S}| \tilde{S}_{ij} f_m(\tilde{\text{Ri}}). \quad (12)$$

Substituting Eqs. (4) and (12) into Eq. (11) results in

$$L_{ij} = C_S^2 M_{ij}, \quad (13)$$

with

$$M_{ij} = 2\Delta^2 [|\tilde{S}| \widetilde{\bar{S}_{ij} f_m(\text{Ri})} - 4\beta |\tilde{S}| \tilde{S}_{ij} f_m(\tilde{\text{Ri}})]. \quad (14)$$

Here, the tilde in the first term in square brackets extends over all three factors forming the product. The parameter β is defined as

$$\beta = \frac{C_{S(2\Delta)}^2}{C_S^2}, \quad (15)$$

and so it denotes the scale dependence of the C_S parameter. A scale-invariant model corresponds to the choice of $\beta = 1$. To implement the dynamic procedure at two different scales, a working assumption is made stating that in the Germano identity the tensor terms relating to the test-filter scale are significantly greater than the terms relating to the grid-filter scale (see Bou-Zeid et al. 2005). Therefore, initially setting $\beta = 1$ in Eq. (14) results in

$$L_{ij} \approx C_{S(2\Delta)}^2 M_{ij}. \quad (16)$$

Equation (16) describes an overdetermined system. Lilly (1992) proposed a least squares approach for the minimization of the squared error ($e_{ij} e_{ij}$) arising from the use of the Smagorinsky model in Eq. (11):

$$e_{ij} e_{ij} = [L_{ij} - C_{S(2\Delta)}^2 M_{ij}]^2, \quad (17)$$

which leads to

$$C_{S(2\Delta)}^2 = \frac{\langle L_{ij} M_{ij} \rangle}{\langle M_{ij} M_{ij} \rangle}. \quad (18)$$

Repeated indices are to be contracted. Angle brackets here indicate an averaging procedure, which also serves to reduce the large variability of C_S in time and space, leading to improved numerical stability.

A second test filter scale can be introduced at 4Δ according to Porté-Agel et al. (2000) (see also Bou-Zeid et al. 2005) to account for the scale dependency of the SGS turbulence mixing length through the estimation of β . Applying the same dynamic procedure as above results in

$$C_{S(4\Delta)}^2 = \frac{\langle Q_{ij} N_{ij} \rangle}{\langle N_{ij} N_{ij} \rangle}, \quad (19)$$

where

$$Q_{ij} = \widehat{\bar{u}_i \bar{u}_j} - \hat{u}_i \hat{u}_j \quad (20)$$

and

$$N_{ij} = 2\Delta^2 [|\hat{S}| \widehat{\bar{S}_{ij} f_m(\text{Ri})} - 16\beta^2 |\hat{S}| \hat{S}_{ij} f_m(\hat{\text{Ri}})], \quad (21)$$

with the caret denoting filtering at the scale 4Δ .

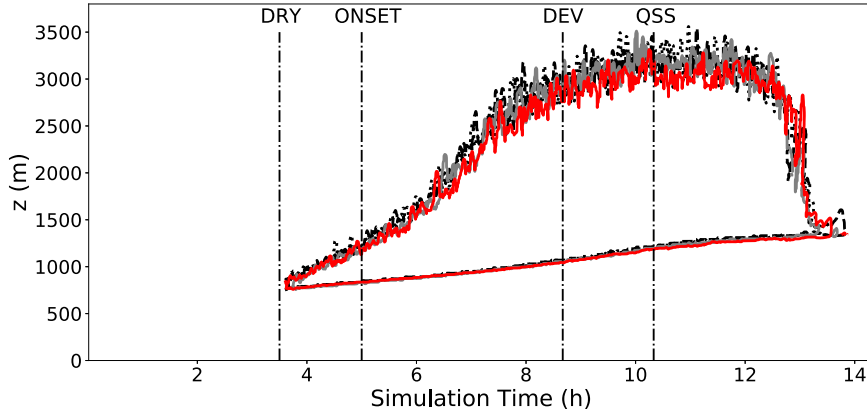


FIG. 1. Evolution of cloud-base and cloud-top (cloud cover ≥ 0.001) height in time from the SMAG $\Delta x = 25$ m (red), SMAG $\Delta x = 50$ m (gray), LASD $\Delta x = 50$ m (dashed black), and LocASD $\Delta x = 50$ m (dotted black) ARM simulations. The vertical dash-dotted lines depict selected points in time that represent different stages of the BL and cloud development.

Porté-Agel et al. (2000) estimated β by constructing a polynomial from the different tensors, assuming that the parameter β is scale invariant, i.e.,

$$\beta = \frac{C_{S(4\Delta)}^2}{C_{S(2\Delta)}^2} = \frac{C_{S(2\Delta)}^2}{C_S^2}, \quad (22)$$

and therefore,

$$\beta^2 = \frac{C_{S(4\Delta)}^2}{C_S^2}. \quad (23)$$

Here, we adopt this assumption but we follow the Bou-Zeid et al. (2005) approach where β is calculated using Eq. (22) after initially setting $\beta = 1$ in Eqs. (14) and (21) as mentioned above and depicted in Eq. (16) (and similarly for scales 4Δ). Evaluating the Smagorinsky coefficient at the two filter scales by means of Eqs. (18) and (19), the β parameter is calculated in practice by taking

$$\beta = \max \left[\frac{C_{S(4\Delta)}^2}{C_{S(2\Delta)}^2}, 0.125 \right], \quad (24)$$

where a minimum value is set to avoid numerical instabilities when β tends to 0 (see Bou-Zeid et al. 2005). The Smagorinsky coefficient used at the grid scale is obtained from

$$C_S^2 = \frac{C_{S(2\Delta)}^2}{\beta}. \quad (25)$$

Dynamic model for the SGS Prandtl number

A second tunable parameter, the SGS Prandtl number (Pr), is present in the SGS scalar flux models [Eqs. (9) and (10)]. The Germano identity can be applied again in the heat flux equation at scale 2Δ as

$$H_j = T_{\theta j} - \bar{\tau}_{\theta j} = \widetilde{\widetilde{u_j \theta}} - \widetilde{\widetilde{u_j} \theta}, \quad (26)$$

where $T_{\theta j}$ is the SGS heat flux eddy-diffusivity scheme implemented at the same scale:

$$T_{\theta j} = -C_{\theta(2\Delta)}(2\Delta)^2 |\widetilde{S}| \frac{\partial \widetilde{\theta}}{\partial x_j} f_h(\widetilde{Ri}). \quad (27)$$

The resolved heat flux (H_j) represents fluxes at scales intermediate to 2Δ and Δ . The scalar dynamic model aims to predict the coefficient C_θ , which equals

$$C_\theta = \frac{C_S^2}{Pr}. \quad (28)$$

Thus, following the same dynamic procedure as for momentum at scales 2Δ we have

$$C_{\theta(2\Delta)} = \frac{\langle H_j R_j \rangle}{\langle R_j R_j \rangle}, \quad (29)$$

with R_j

$$R_j = \Delta^2 \left[\widetilde{\left| \widetilde{S} \right| \frac{\partial \widetilde{\theta}}{\partial x_j} f_h(\widetilde{Ri})} - 4\beta_\theta |\widetilde{S}| \frac{\partial \widetilde{\theta}}{\partial x_j} f_h(\widetilde{Ri}) \right], \quad (30)$$

and the scale-dependency parameter (β_θ) for the C_θ coefficient is given by

$$\beta_\theta = \frac{C_{\theta(2\Delta)}}{C_\theta}. \quad (31)$$

For scales 4Δ , respectively,

$$C_{\theta(4\Delta)} = \frac{\langle F_j X_j \rangle}{\langle X_j X_j \rangle}, \quad (32)$$

and

$$F_j = \widetilde{\widetilde{u_j \theta}} - \widehat{\widehat{u_j} \theta}, \quad (33)$$

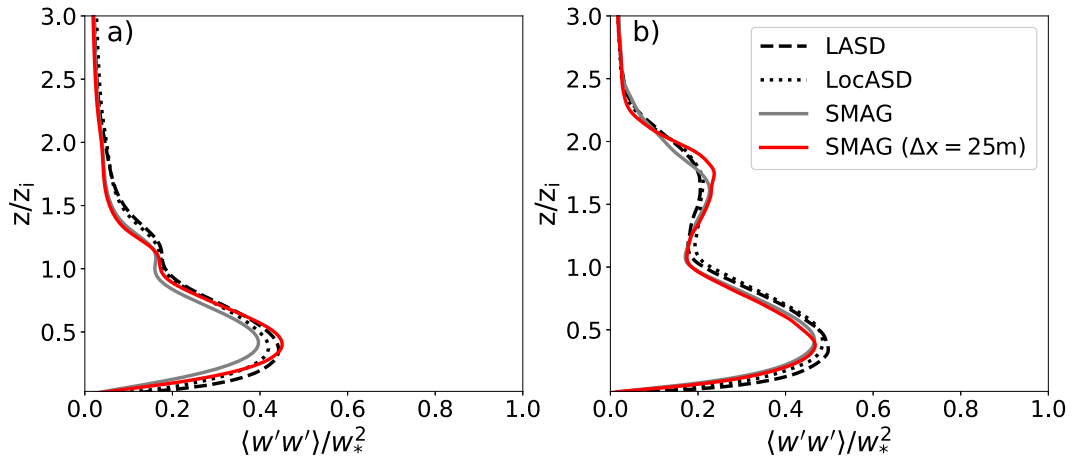


FIG. 2. Vertical profiles of planar-averaged resolved vertical velocity variance ($\langle w'w' \rangle$), normalized by the convective vertical velocity (w_*) at (a) ONSET and (b) DEV times for the different SMAG, LASD, and LocASD runs as in Fig. 1. z_i is the BL height specified at the height of minimum heat flux.

$$X_j = \Delta^2 \left[\overline{\left| \frac{\partial \theta}{\partial x_j} \right|} f_h(\text{Ri}) - 16\beta_\theta^2 \widehat{|\bar{S}|} \frac{\partial \theta}{\partial x_j} f_h(\text{Ri}) \right], \quad (34)$$

$$C_\theta = \frac{C_{\theta(2\Delta)}}{\beta_\theta}. \quad (35)$$

As in Eq. (24), β_θ is calculated setting the same lower bound:

$$\beta_\theta = \max \left[\frac{C_{\theta(4\Delta)}}{C_{\theta(2\Delta)}}, 0.125 \right]. \quad (36)$$

3) AVERAGING PROCEDURES

(i) LASD

In the derivation of the dynamic Smagorinsky model, C_S is left outside the filtering operation [see Eqs. (13) and (14)] assuming that the coefficient has minimal spatial variation compared to the filter scale. This approximation leads to numerical instabilities during the dynamic calculations. As mentioned above, Lilly (1992) proposed an error minimization approach based on plane averaging over homogeneous directions of the flow (see also Germano et al. 1991). However, horizontal averaging cannot capture the spatial variations of mixing in inhomogeneous flows. Therefore, Meneveau et al. (1996) suggested a Lagrangian averaging operation for some test quantity $A(\mathbf{x}, t)$ along the fluid-particle trajectories according to

$$\langle A(\mathbf{x}, t) \rangle = \int_{-\infty}^t A[\mathbf{x}(t'), t'] W(t - t') dt'. \quad (37)$$

Here $\mathbf{x}(t')$ is the position along the trajectory at the earlier time t' and $W(t - t')$ is a weighting function. By choosing $W(t - t') = T^{-1} e^{-(t-t')/T}$, Eq. (37) becomes the solution of a relaxation equation that can be approximated in a discrete form by (Meneveau et al. 1996)

$$\frac{\langle A(\mathbf{x}) \rangle^{n+1} - \langle A(\mathbf{x} - \mathbf{u}^n \delta t) \rangle^n}{\delta t} = \frac{1}{T^n} \{ [A(\mathbf{x})]^{n+1} - \langle A(\mathbf{x}) \rangle^{n+1} \}, \quad (38)$$

which by rearranging becomes

$$\langle A(\mathbf{x}) \rangle^{n+1} = \epsilon [A(\mathbf{x})]^{n+1} + (1 - \epsilon) \langle A(\mathbf{x} - \mathbf{u}^n \delta t) \rangle^n, \quad (39)$$

where

$$\epsilon = \frac{\delta t / T^n}{1 + \delta t / T^n}. \quad (40)$$

Therefore, Eq. (39) solves for the updated ($n + 1$) averaged value of A as a weighted sum of the current A source term ($n + 1$) at grid point \mathbf{x} and the interpolated prior value at n .

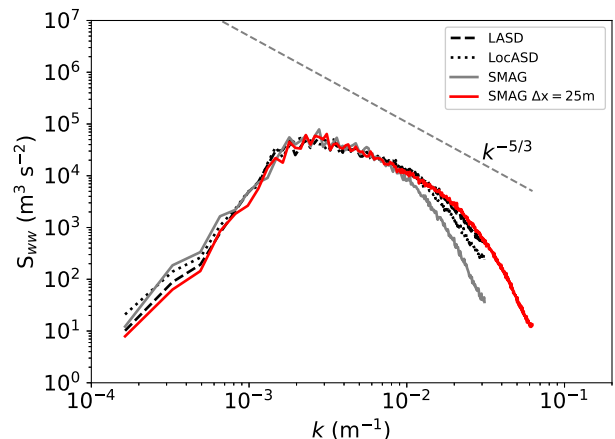


FIG. 3. Two-dimensional vertical velocity spectra in the middle of the BL ($z = 260$ m) from the LASD, LocASD, SMAG 50 m simulations, and SMAG 25 m run at the ONSET stage. Gray dashed line shows the idealized $k^{-5/3}$ spectrum.

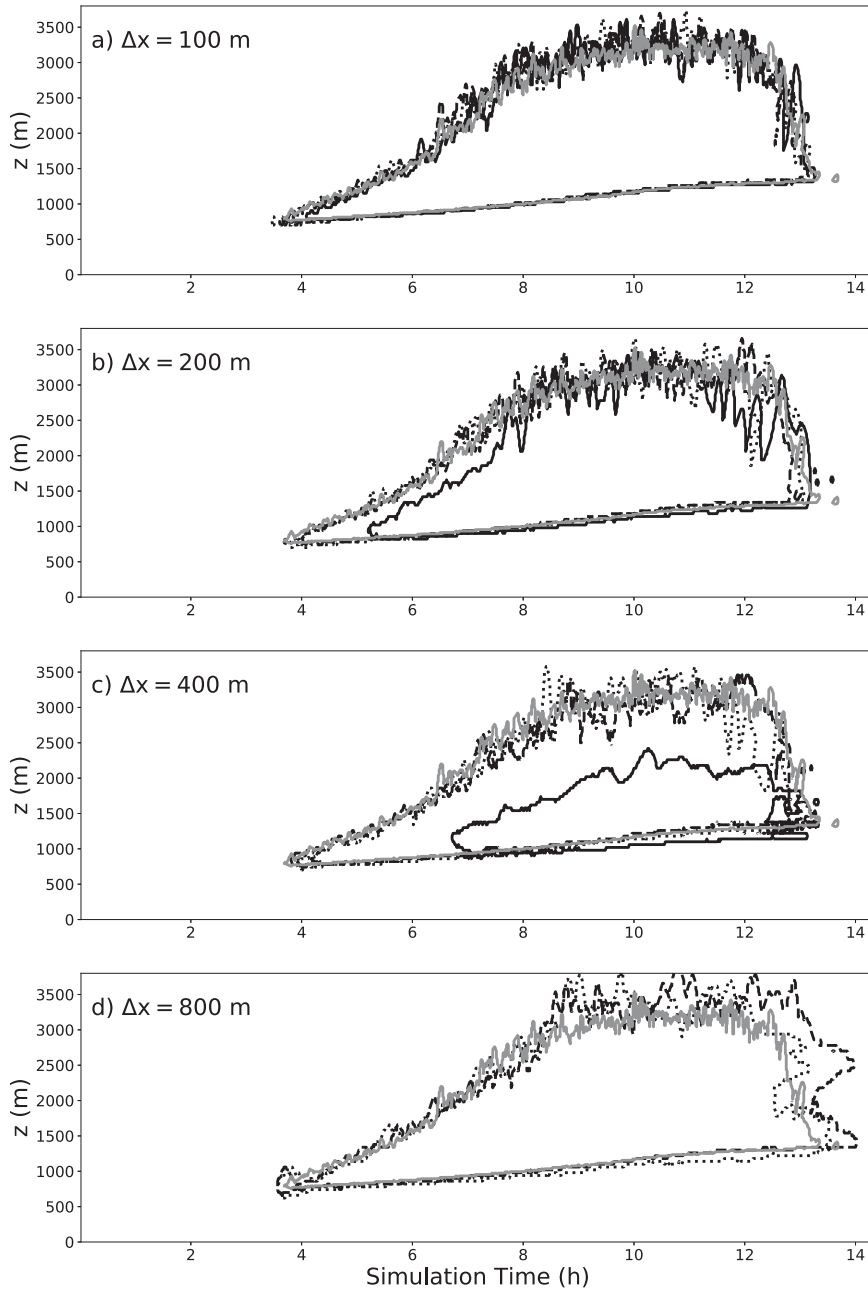


FIG. 4. Evolution of cloud-base and cloud-top (cloud cover ≥ 0.001) height in time (hours since the start of the simulation) from the LES (solid gray lines), SMAG (solid black lines), LASD (dashed black lines), and LocASD (dotted black lines) simulations using different horizontal grid resolutions (Δx) (a) 100, (b) 200, (c) 400, and (d) 800 m.

More specifically, δt is the Lagrangian time step which depends on how often the dynamic model is called during the MONC run; here, it is taken as 5 times the model time step ($5\Delta t$) and $\langle A(\mathbf{x} - \mathbf{u}^n \delta t) \rangle^n$ is the value of the averaged quantity A at its upstream location at the previous time step (n) and is estimated by trilinear interpolation. T^n is the time scale that controls the memory length of the Lagrangian averaging. It represents time scales related to the smallest resolved

eddies. Meneveau et al. (1996) proposed the following time scale on dimensional grounds:

$$T^n = \phi \Delta [\langle L_{ij} M_{ij}(\mathbf{x}) \rangle^n \langle M_{ij} M_{ij}(\mathbf{x}) \rangle^n]^{-1/8}, \quad (41)$$

choosing $\phi = 1.5$ based on the Lagrangian autocorrelation function of the contracted tensors. For scales 4Δ Eq. (41) is

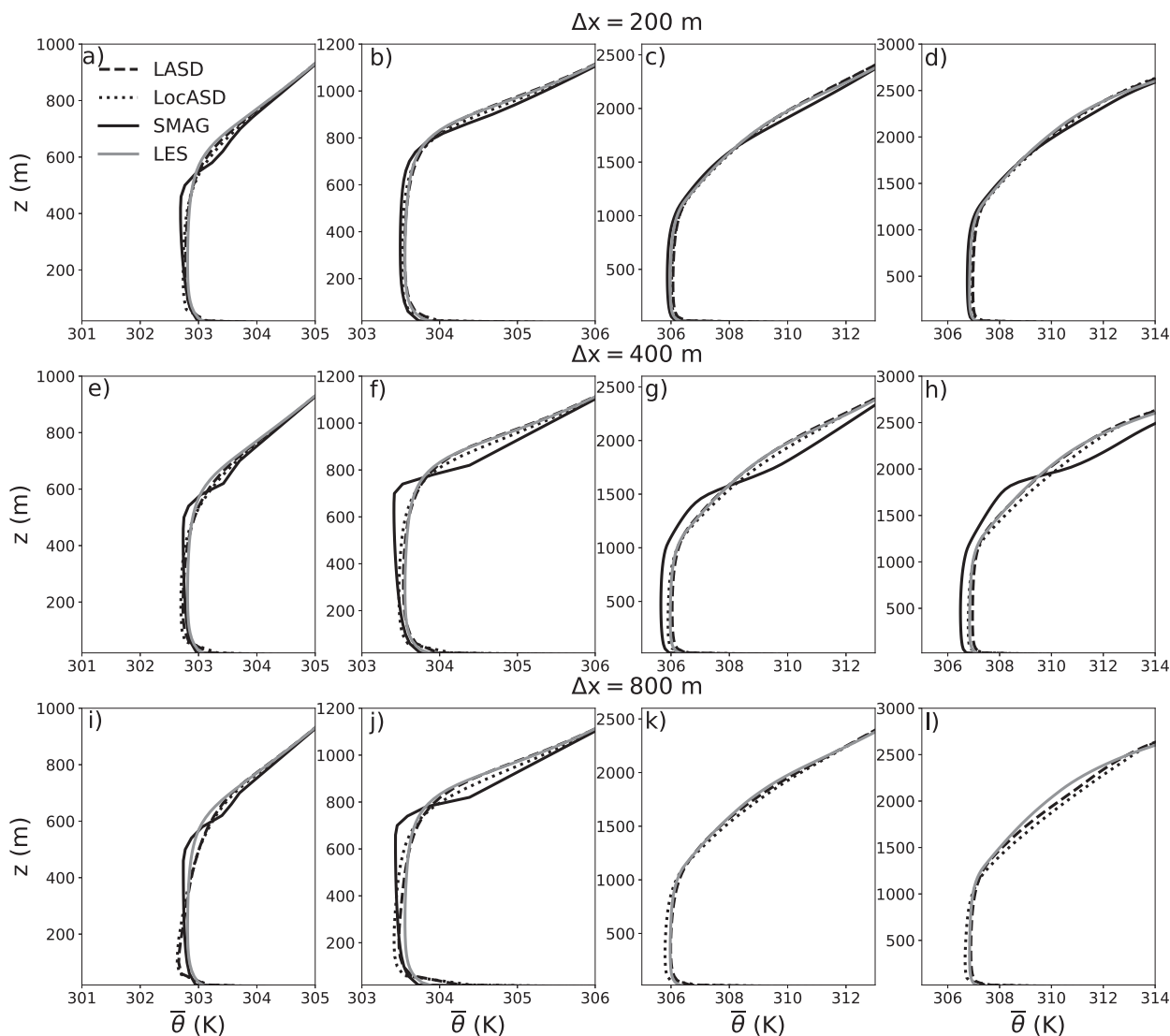


FIG. 5. Planar-averaged profiles of potential temperature ($\bar{\theta}$) from the LES, SMAG, LASD, and LocASD simulations using different horizontal grid resolutions, specified at four different stages during the simulation: (a) 200 m DRY, (b) 200 m ONSET, (c) 200 m DEV, (d) 200 m QSS, (e) 400 m DRY, (f) 400 m ONSET, (g) 400 m DEV, (h) 400 m QSS, (i) 800 m DRY, (j) 800 m ONSET, (k) 800 m DEV, and (l) 800 m QSS. Note that for the 800 m SMAG run there are no profiles for (k) and (l) as the simulation crashed.

formulated using the relevant quantities [$\langle Q_{ij}N_{ij}(\mathbf{x}) \rangle$ and $\langle N_{ij}N_{ij}(\mathbf{x}) \rangle$, respectively]. We also adopt a Lagrangian time scale (T_θ) from [Stoll and Porté-Agel \(2008\)](#) for the calculation of C_θ :

$$T_\theta^n = \phi \Delta \sigma_\theta [(H_j R_j(\mathbf{x}))^n \langle R_j R_j(\mathbf{x}) \rangle^n]^{-1/4}, \quad (42)$$

with σ_θ the standard deviation of potential temperature at each vertical level. As for the momentum Lagrangian time scale, T_θ^n is calculated with the appropriate scalars for scales 4Δ .

Negative values of the averaged scalar quantities that involve the resolved tensors are clipped to zero to avoid negative coefficients (diffusivity) values. However, as these tend to zero

the Lagrangian time scale becomes very large [see Eq. (41)], ensuring the method is sampling away from zero (negative) local values.

(ii) Locally Averaged Scale-dependent Dynamic model

[Basu and Porté-Agel \(2006\)](#) introduced local averaging in the [Porté-Agel et al. \(2000\)](#) scale-dependent dynamic model for a better representation of turbulence intermittency and variability in the stable BL. Nevertheless, they used planar averaging to determine the β parameter through solving a fifth-order polynomial. Attempts to employ local averaging to calculate β resulted in unstable solutions (see [Stoll and Porté-Agel 2008](#)). Here, we also apply the local averaging approach to the dynamic, scale-dependent Smagorinsky

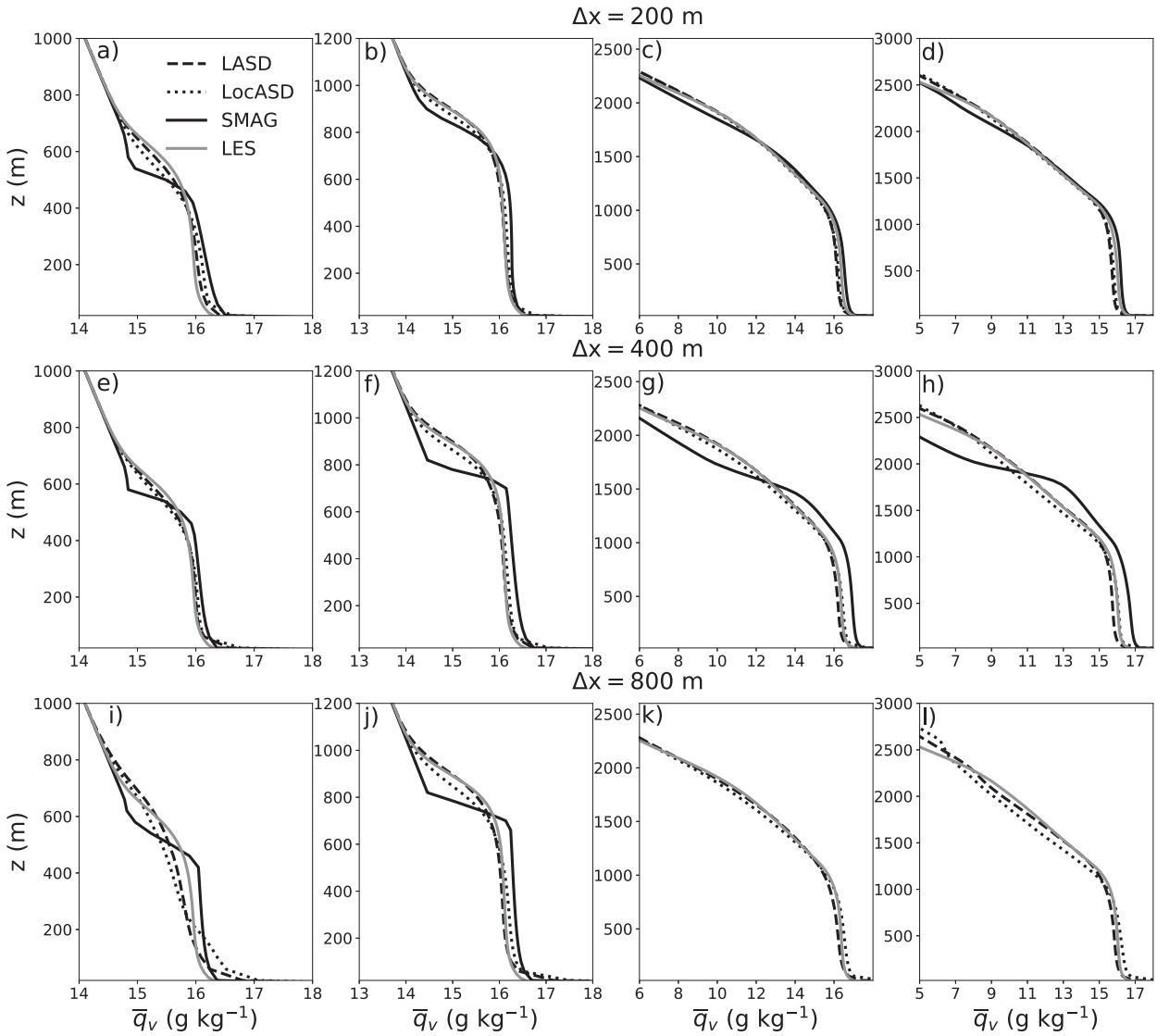


FIG. 6. As in Fig. 5, but for water vapor mixing ratio (\bar{q}_v).

model, as described in section 2 above, where any averaged quantity $\langle A \rangle$ is given by

$$\langle A(x, y) \rangle = \frac{1}{(2m + 1)^2} \sum_{i=-m}^m \sum_{j=-m}^m A(x + i, y + j), \quad (43)$$

which express a moving average over a horizontal stencil of 3×3 neighboring grid points ($m = 1$) along the x and y directions. Clipping here is much more invasive compared to LASD as any negative values of $\langle A \rangle$ are set to zero. The locally Averaged, Scale-dependent Dynamic model (LocASD) is introduced and tested as simpler and computationally less expensive alternative compared to the Lagrangian-averaged approach (LASD). It should be noted that the local averaging formulation implemented here as a different flavor of LASD and does not follow the formulation of Basu and Porté-Agel

(2006) and Basu et al. (2008), especially in terms of estimating the β factor.

3. Simulations

The scale-dependent dynamic Smagorinsky model, with the two averaging approaches (LASD and LocASD), was implemented in MONC and used to simulate the diurnal cycle of shallow cumuli over the ARM Program site on 21 June 1997. This case study, based on an idealization of available observations, served as a test bed for the LES model intercomparison study of Brown et al. (2002). Development of cumulus convection over land can prove a challenging task for numerical modeling, especially away from the LES resolution regime, as it involves evolving turbulence length scales in the BL and cloud layer that are represented by partially resolved structures. Only a few attempts have been made to simulate cloudy BLs

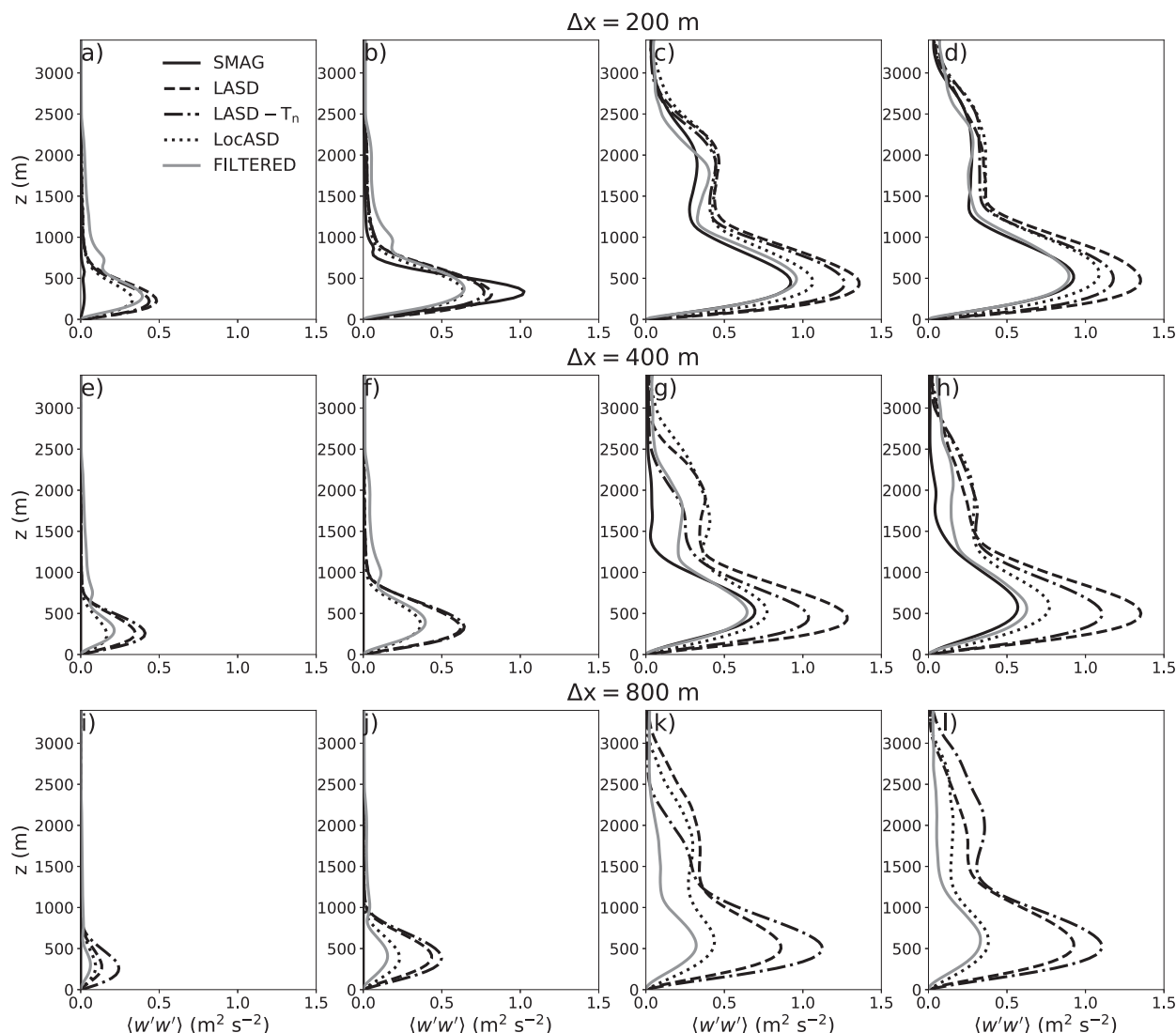


FIG. 7. As in Fig. 6, but for the resolved vertical velocity variance ($\langle w'w' \rangle$). The gray solid lines show the LES vertical velocity variance coarse-grained (FILTERED) at the corresponding resolutions. Note that besides planar averaging these values have also been averaged over a 600 s window.

using dynamic models, mainly focusing on stratocumulus cases (Kirkpatrick et al. 2006; Shi et al. 2018). Here, we will apply the dynamic Smagorinsky scheme in simulating developing shallow cumuli for the first time while pushing this approach beyond LES resolutions.

The dynamic model was compared against the conventional Smagorinsky scheme (SMAG) at a range of horizontal grid spacings (Δx), from the LES regime ($\Delta x = 50$ m) and the near-gray-zone to the gray-zone regime ($\Delta x = 800$ m) for the whole simulation period. The reference LES simulation was conducted using the Smagorinsky scheme with $\Delta x = 50$ m and a vertical grid spacing of $\Delta z = 20$ m over a 19.2×19.2 km² domain. A second SMAG simulation with $\Delta x = 25$ m and $\Delta z = 10$ m was conducted for comparison in the LES regime. The domain top was set as a rigid lid at 4400 m while gravity wave damping was applied above 3000 m. The initial

conditions follow Brown et al. (2002) and the simulations were run for 14 h, starting from 0530 to 1930 local time. The simulation is solely forced by the time-varying surface sensible and latent heat fluxes as the impact of large-scale forcing is negligible (see Brown et al. 2002). A geostrophic wind of $U_g = 10$ m s⁻¹ was chosen to represent the large-scale pressure gradient over the simulation area. Coarser simulations were run at $\Delta x = 100, 200, 400,$ and 800 m keeping the vertical resolution to $\Delta z = 40$ m similar to that used in operational and high-resolution mesoscale models. The 800 m simulations were conducted using double the domain size in both directions (48×48 grid points) to ensure an adequate number of grid points in the simulation domain.

a. ARM LES benchmark

The cloud-base and cloud-top height from the LES runs are shown in Fig. 1. Clouds form at about 4 h after the start of the

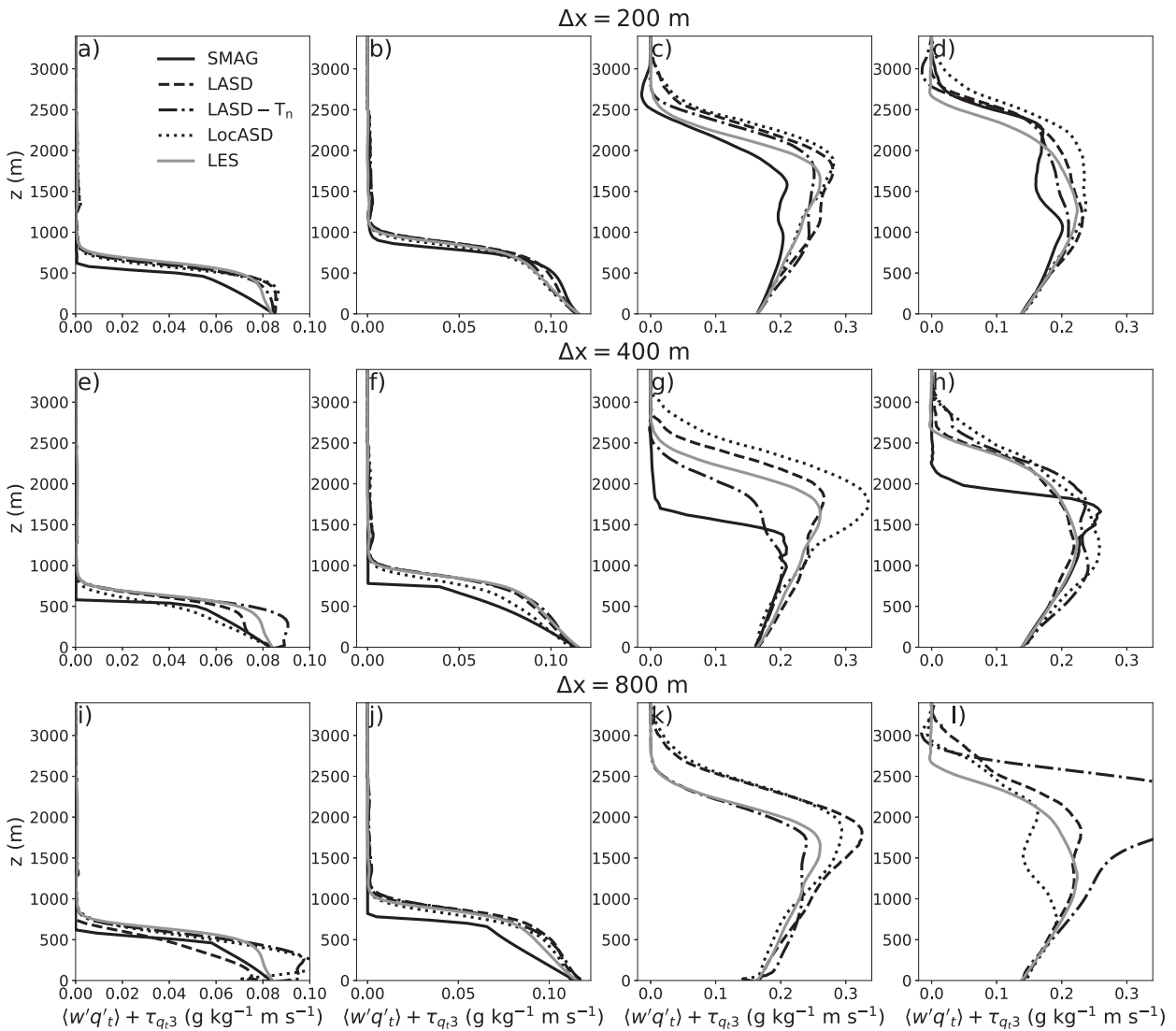


FIG. 8. As in Fig. 5, but for the total (resolved + SGS) water mixing ratio flux ($\langle w'q'_t \rangle + \tau_{q,3}$).

simulation, progressing to an active development stage and then to a maximum cloud height of about 3000 m, before clouds dissipate near the end of the simulation. For the rest of the paper our analysis will focus on four different times representative of the phases of BL and cloud development during the simulation, as identified in Fig. 1: the early morning BL development just before cloud formation (DRY), the onset of passive clouds (ONSET), the rapid cloud development stage (DEV), and a quasi-steady state where the cloud top remains fairly constant (QSS). The aim is to test the ability of the conventional and dynamic Smagorinsky in representing turbulent transfer at a range of subkilometer resolutions and subsequent cloud development.

Only small differences exist among the $\Delta x = 50$ m simulations and the 25 m SMAG run in Fig. 1, suggesting that they are close to the LES converging regime (Pope 2000; Sullivan and Patton 2011). Nonetheless, the 25 m run systematically

produces slightly lower maximum cloud tops probably due to the finer vertical resolution. Cloud onset, development and dissipation are occurring at the same time in all LES runs. The converging behavior is also evident in Fig. 2 which shows the planar-averaged resolved w variance at the ONSET and DEV stages. The dynamic and SMAG 25 m runs produce slightly stronger turbulent fluctuations in the BL compared to the SMAG 50 m simulation at the ONSET stage (Fig. 2a) before becoming almost identical at the DEV stage.

Even though the overall differences are small, the impact of the SGS mixing length scale is still evident at the LES resolution regime. Following Mason (1989), C_S can be interpreted as λ/Δ which implies that the SGS mixing length acts like a filter that partially determines the model's effective resolution. In fact, maximum λ values in the BL at ONSET are quite similar between LASD (6.31 m) and SMAG 25 m run (5.75 m) in relation to the SMAG 50 m simulation

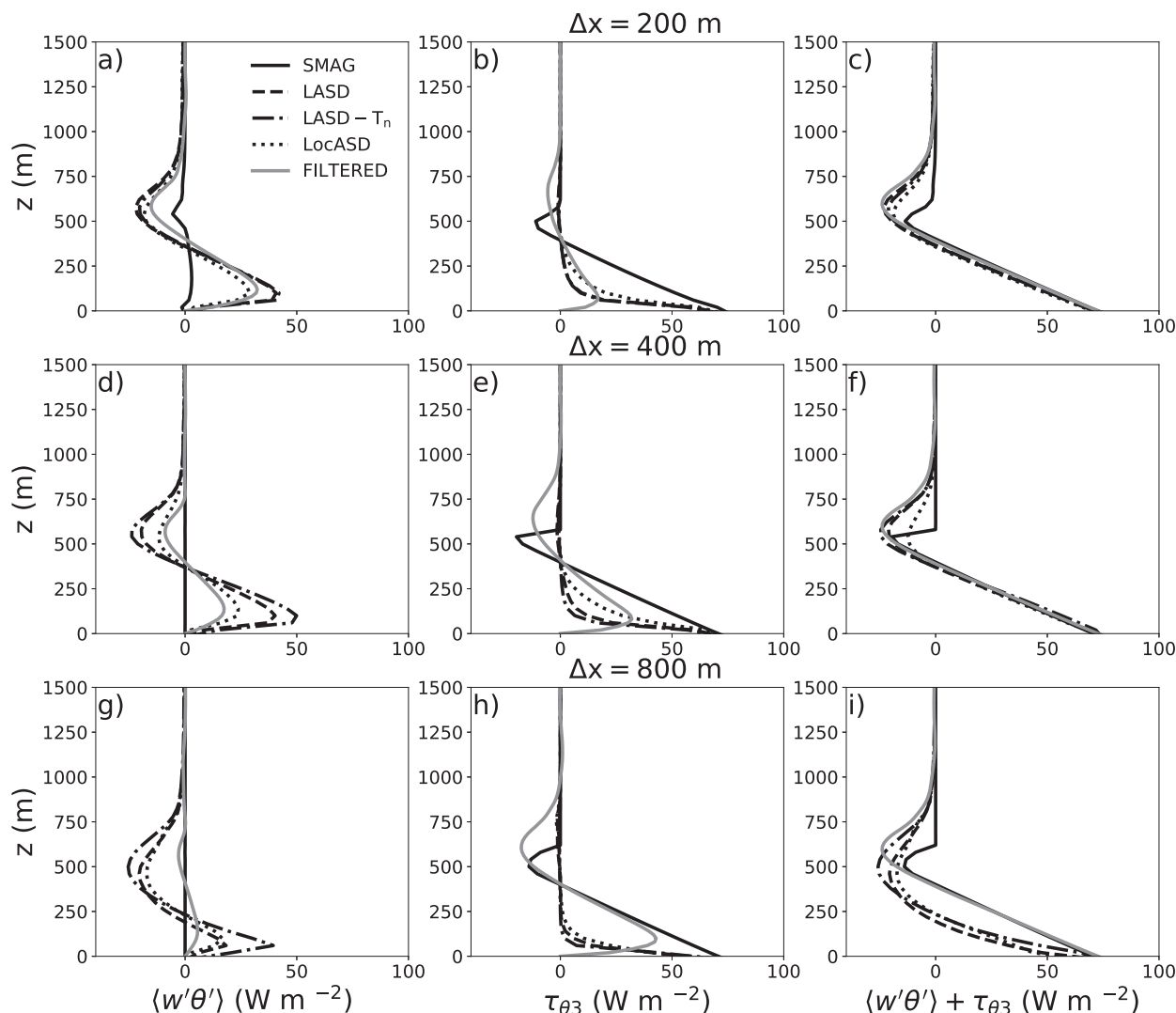


FIG. 9. As in Fig. 7, but for the total (resolved + SGS) sensible heat flux ($\langle w'\theta' \rangle + \tau_{\theta 3}$) during the DRY stage.

(11.50 m). This is corroborated by examining the 2D vertical velocity spectra in Fig. 3, where SMAG 25 m is producing fairly similar spectra to LASD and LocASD in the middle of the BL as opposed to the SMAG 50 m, which exhibits stronger dissipation imposed by the SGS turbulence scheme (LocASD shows a slightly faster drop off from the idealized inertial subrange compared to LASD as maximum LocASD $\lambda = 8.46$ m).

Moreover, these early differences can be traced back to the first hour of the simulation when the BL is stable. LASD and LocASD are closer to the SMAG 25 m run (not shown) compared to SMAG 50 m (see also the discrepancy between the SMAG 50 m and other runs in Fig. 2a). This can be attributed to the simulation moving substantially away from the LES regime under stable stratification, leading to poor SMAG behavior at $\Delta x = 50$ m (see also Basu and Porté-Agel 2006), but it does not affect the further evolution of the convective BL (CBL) and subsequent cloud development.

b. Gray-zone ARM simulations

1) SHALLOW CUMULI DEVELOPMENT

Figure 4 shows the cloud-base and cloud-top height evolution from the $\Delta x = 100$ to 800 m SMAG, LASD, and LocASD simulations. Even from the $\Delta x = 100$ m some differences become apparent among the simulations. The SMAG run exhibits a slight delay in the initiation of clouds (of about 0.5 h) which is related to the late spinup of turbulence compared to the dynamic model runs (LASD and LocASD). As shown in Efstathiou et al. (2018), during the early CBL development, the $\Delta x = 100$ m simulation can be in the near-gray zone causing a delay in the spinup of resolved motions. In fact, the scaling parameter Δ/z_i (where z_i is the BL depth) spans from 0.5 to 0.125 during the DRY stage, indicating that the simulations are mainly in the near-gray-zone regime (see also Honnert et al. 2020). In any case, the errors related to late DRY CBL evolution do not significantly

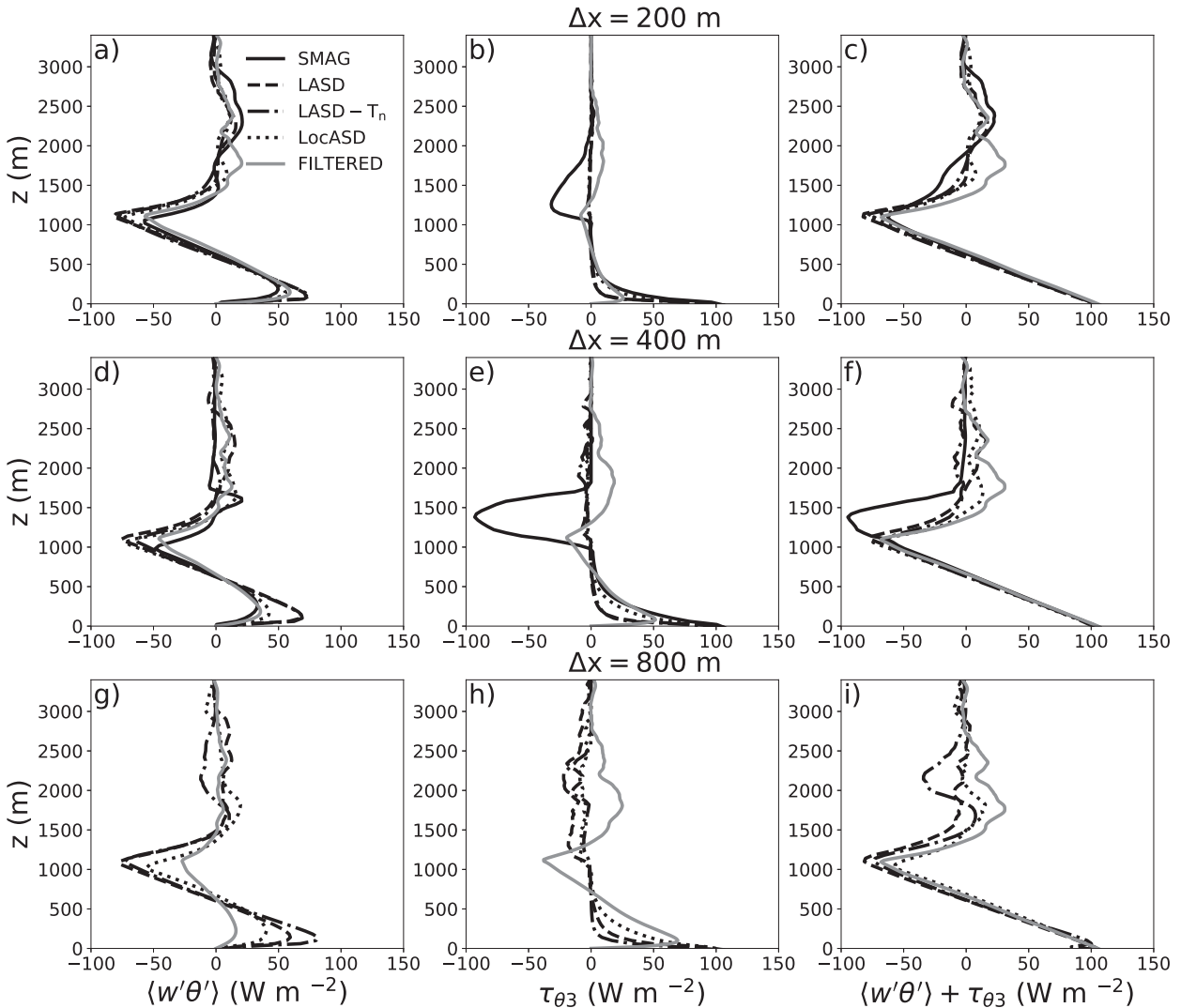


FIG. 10. As in Fig. 9, but for the DEV stage.

affect the subsequent shallow cumuli development in the SMAG $\Delta x = 100$ m.

At $\Delta x = 200$ m (Fig. 4b) the differences between SMAG and the LES become much more pronounced, with SMAG exhibiting a 1.5 h delay in cloud formation (see also Petch et al. 2002). Furthermore, cloud development is also significantly delayed compared to the LES, matching the LES evolution only at the end of the DEV stage. In contrast, both LASD and LocASD are able to capture the cloud initiation and development, closely following the LES results. Cloud-top height variability is more distinct in the dynamic runs compared to the LES, especially for the LocASD run which produces slightly higher tops during the QSS stage.

Moving to coarser resolutions ($\Delta x = 400$ m), the early stages of the ARM simulation are firmly found into the gray zone resulting in a more substantial delay in cloud onset and faster cloud dissipation for the conventional SMAG run (Fig. 4c). Cloud tops remain at very low levels throughout the simulation

with no clear stages of cloud evolution and development, suggesting an unrealistic representation of shallow cumulus convection (see Petch et al. 2002) for SMAG. Moreover, cloud base appears consistently lower compared to the LES especially during the QSS stage. The dynamic models follow the LES evolution showing no real resolution dependency on the predicted cloud-base and cloud-top height. Nevertheless, LASD and LocASD exhibit more noticeable cloud-top variability, with LocASD producing strong cloud-top overshooting during the DEV stage and collapses near the end of the simulation.

The SMAG $\Delta x = 800$ m simulation pushes even farther into the gray zone (with $\Delta/z_i \sim 1$ during DEV and QSS stages) and fails to produce any condensation (Fig. 4d) as it crashes after about 8 h from the start of the simulation (see also Petch et al. 2002). The dynamic models continue to provide a fairly accurate representation of cloud evolution compared to the LES. However, some discrepancies between the dynamic runs and the LES are becoming more evident. Condensation occurs

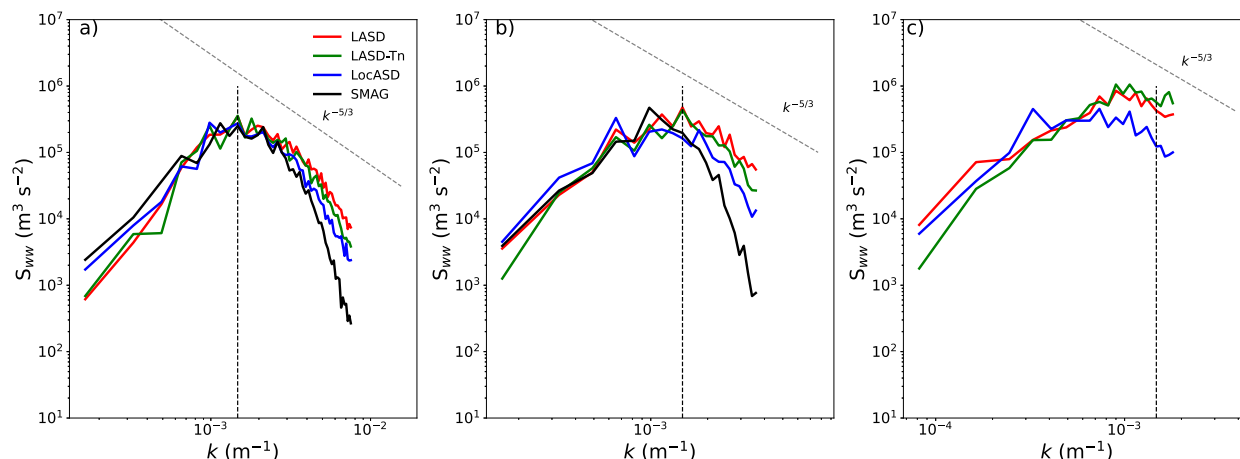


FIG. 11. Two-dimensional vertical velocity spectra at $z = 600$ m for the LASD, LocASD, SMAG, and LASD-Tn simulations at (a) 200, (b) 400, and (c) 800 m during the DEV stage. Gray dashed line shows the idealized $k^{-5/3}$ spectrum while the black dashed line the position of the peak from the LES spectra.

earlier for LASD and LocASD, while cloud tops are systematically higher with LASD maintaining condensation for longer toward the end of the simulation.

2) MEAN PROFILES

Planar-averaged profiles of potential temperature, water vapor mixing ratio, and vertical velocity variance are shown in Figs. 5–7, respectively, from the 200, 400, and 800 m simulations, at four times during the DRY, ONSET, DEV, and QSS stages. The vertical velocity variance profiles are also time averaged over a 600 s window to provide more flow realizations (cloud samples) in the cloud layer. Additionally, Fig. 7 contains the w variance from the coarse-grained (filtered) LES fields for comparison, following the approach of Honnert et al. (2011). Included in Fig. 7 is a simulation introducing a different T^n that will be presented in a later section of the paper.

Starting from the 200 m run, SMAG produces a superadiabatic potential temperature profile during the DRY BL stage (Fig. 5a), with a lower and moister BL (Fig. 6) compared to the LES. This behavior is typical of the lack of resolved turbulent transfer at gray-zone resolutions (see Efsthathiou et al. 2016; Simon et al. 2019) as can be seen in Fig. 7 where SMAG does not produce any resolved overturning at the DRY stage. Even though SMAG eventually spins up during the ONSET stage, moisture is still confined in the slightly lower and cooler BL (Figs. 5b and 6b).

At $\Delta x = 400$ m SMAG issues are exaggerated and the BL representation is further deteriorated as resolution becomes coarser. Super adiabatic temperature profiles are maintained for longer (Figs. 5e,f), while the BL remains cooler and moister throughout the simulation in comparison to the LES. The lack of resolved fluxes up until the DEV stage, as shown in Fig. 7f, confines most of the moisture in the BL (see Fig. 8f), whereas the lack of vertical entrainment (due to not producing any convective overturning) results in the significantly cooler BL. This leads to a lower cloud base compared to the LES as seen in Fig. 4c. Despite the

initiation of resolved turbulence there is no substantial increase of the vertical velocity variance in the cloud layer (Figs. 7g,h), which depicts the lack of significant cloud development (Fig. 4c). As mentioned above, the 800 m SMAG run fails to produce any resolved motion or condensation but before it crashes it exhibits similar behavior to the 400 m during the first half of the simulation [see panels (i) and (j) in Figs. 5–8].

The dynamic approaches on the other hand can clearly better reproduce the mean LES profiles. Temperature and moisture profiles are well mixed in the BL, exhibiting a warmer (cooler) and drier (moister) BL (cloud layer) in average compared to the SMAG simulations and closely following the LES profiles (Figs. 5 and 6). Moreover, LASD and LocASD simulations seem to spin up on time in contrast to the worsening spinup issues of SMAG with coarsening resolution (see Fig. 7).

However, there are some differences between the LASD and LocASD runs and both dynamic approaches with the LES, especially at coarser resolutions. LASD is significantly more energetic compared to the LES filtered fields, producing stronger turbulent fluctuations in the BL. This becomes more obvious in the 400 and 800 m simulations and mainly during the DEV and QSS stages. More energetic BL structures result in a slightly drier and warmer BL due to stronger entrainment in LASD simulations (Figs. 5 and 6, see also Figs. 9 and 10). Nonetheless, LocASD is capturing the first-order profiles and energetics of the resolved filtered fields across the different resolutions throughout the whole diurnal cycle.

3) TOTAL WATER AND HEAT FLUX PROFILES

The better representation of the first-order quantities from the dynamic approaches is also reflected in the total water flux profiles. Figure 8 shows the planar- and time-averaged (600 s) total water fluxes (SGS and resolved) from all runs and during the different phases of BL and cloud development. LASD and LocASD runs are able to mainly reproduce the

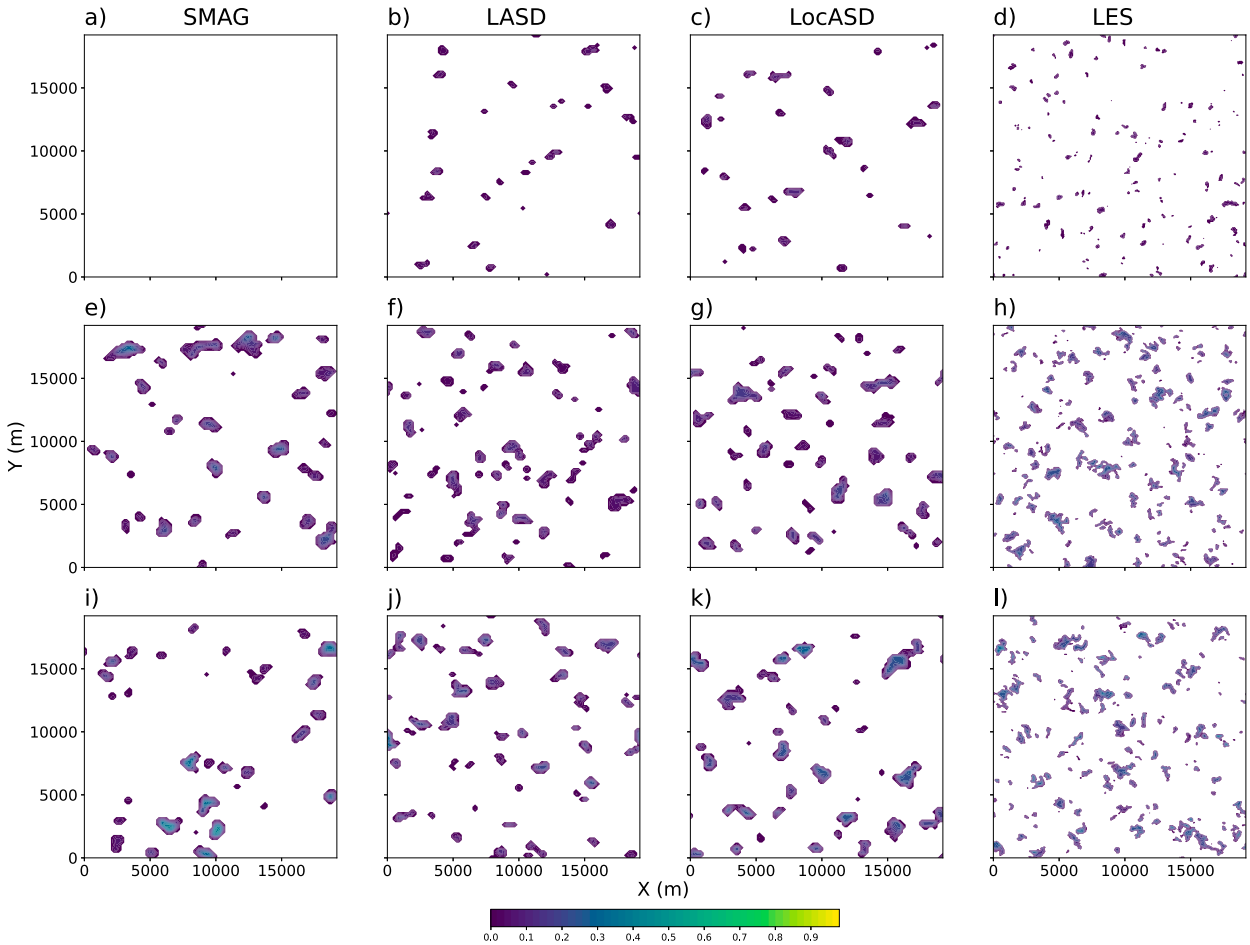


FIG. 12. Horizontal cross section of \bar{q}_l (g kg^{-1}) at height of maximum cloud cover for the $\Delta x = 200$ m run for the (a) ONSET SMAG, (b) ONSET LASD, (c) ONSET LocASD, (d) ONSET LES, (e) DEV SMAG, (f) DEV LASD, (g) DEV LocASD, (h) DEV LES, (i) QSS SMAG, (j) QSS LASD, (k) QSS LocASD, and (l) QSS LES runs. The plots only show grid points where $\bar{q}_l \geq 10^{-6} \text{ g kg}^{-1}$.

total LES transport throughout the BL and the cloud layer for all resolutions (with some small discrepancies present), in contrast to the shallower total water transport in the SMAG simulations. SMAG exhibits significant misrepresentation of the total water flux due to the lack of resolved motion at the early stages of the BL evolution (DRY and ONSET in Figs. 8a,b,e,f), and the strong diffusive water fluxes in the cloud layer (not shown) that determine the shape of total flux profile at later times (DEV and QSS in Figs. 8c,d,g,h). In fact, the establishment of resolved flow at later stages in the SMAG 200 and 400 m runs (Figs. 7c,d,g,h) does not lead to the desired total water turbulent transport compared to the LES. The inaccurate representation of the BL (even at its early stages) and the excessive SGS total water diffusion in the cloud layer as mentioned above causes a significant delay on cloud formation and further development (see Figs. 4b,c). The more accurate representation of turbulent total water transfer in the dynamic runs is reflected on the timings of cloud onset and development, as well as on the modeled cloud-base and cloud-top heights as seen in Fig. 4.

Moreover, LASD and LocASD simulations are able to reproduce the filtered heat flux at the 200 m simulations (Figs. 9a–c) with LASD producing slightly stronger resolved heat fluxes during the DRY stage. At the same time the SMAG run is not resolving any heat flux while the SGS fluxes (Fig. 9b) are unable to produce the right amount of total entrainment heat flux (Fig. 9c). At 400 m, LASD becomes significantly more energetic compared to the filtered fields and LocASD (Fig. 9d) on par with the increased vertical velocity variance in Fig. 7d; however, it is still able to capture the LES total heat flux as shown in Fig. 9f and subsequently reproduce the LES potential temperature profile in Fig. 5e. Both dynamic runs at 800 m depict strong entrainment fluxes that occupy a deeper layer compared to the LES (Fig. 9i). This behavior results in a much warmer upper BL and a stable temperature profile due to the more pronounced entrainment of warm air as shown in Fig. 5i.

During the DEV stage (Fig. 10), LASD exhibits strong resolved heat fluxes in the BL especially at the 400 and 800 m simulations. Moreover, as LASD produces more energetic

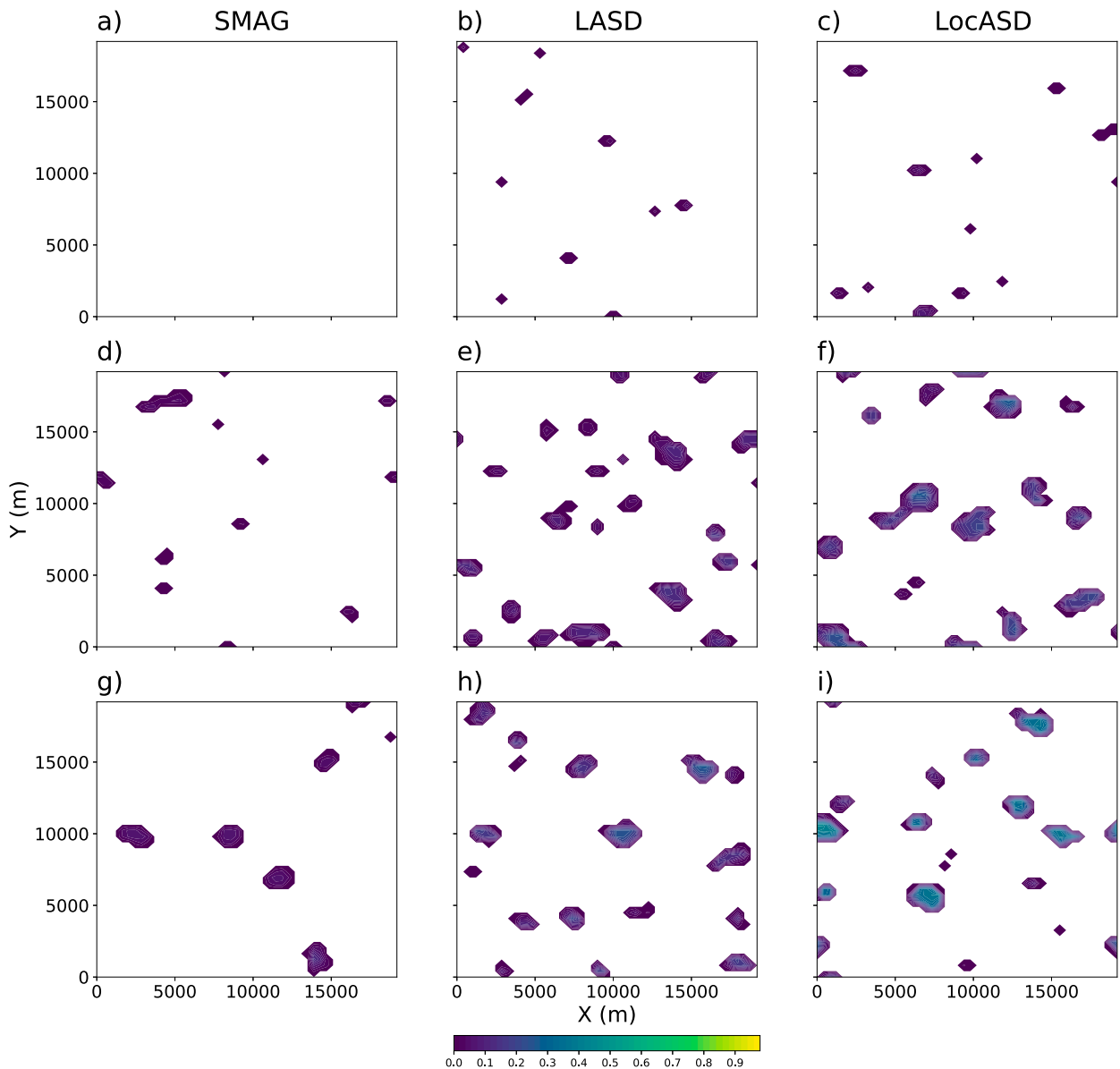


FIG. 13. Horizontal cross section of \bar{q}_l (g kg^{-1}) at height of maximum cloud cover for the $\Delta x = 400$ m run for the (a) ONSET SMAG, (b) ONSET LASD, (c) ONSET LocASD, (d) DEV SMAG, (e) DEV LASD, (f) DEV LocASD, (g) QSS SMAG, (h) QSS LASD, and (i) QSS LocASD runs. The plots only show grid points where $\bar{q}_l \geq 10^{-6} \text{ g kg}^{-1}$.

thermals (see Fig. 7) the entrainment fluxes are stronger, leading to marginally warmer and drier mean BL profiles for LASD during the DEV and QSS stages (this is more obvious at $\Delta x = 200$ m, see Figs. 5 and 6). LocASD seems to follow the filtered LES heat flux fields more closely, similarly to the vertical variance profiles in Fig. 7. In any case, the better agreement with the filtered fields in LocASD does not translate to significant differences in the mean profiles, as the total fluxes are adequately reproduced by both LASD and LocASD.

One important characteristic of the dynamic runs is that they essentially turn off the SGS heat and water transport in the cloud layer by substantially reducing C_θ (increasing Pr).

In contrast, SMAG produces excessive downgradient heat fluxes especially at the 400 m run (Fig. 10e), becoming increasingly dissipative at coarser resolutions. Similarly, vapor diffusion becomes significantly stronger compared to the filtered fields, damping the resolved transport of moisture (not shown). SGS heat and water transport seems to be controlled from the choice of the Pr in the cloud layer. This was confirmed by disabling the dynamic calculation of Pr in the LASD runs which resulted in the deterioration of the simulations, especially in the cloud layer due to the significant increase of SGS heat and moisture fluxes (not shown).

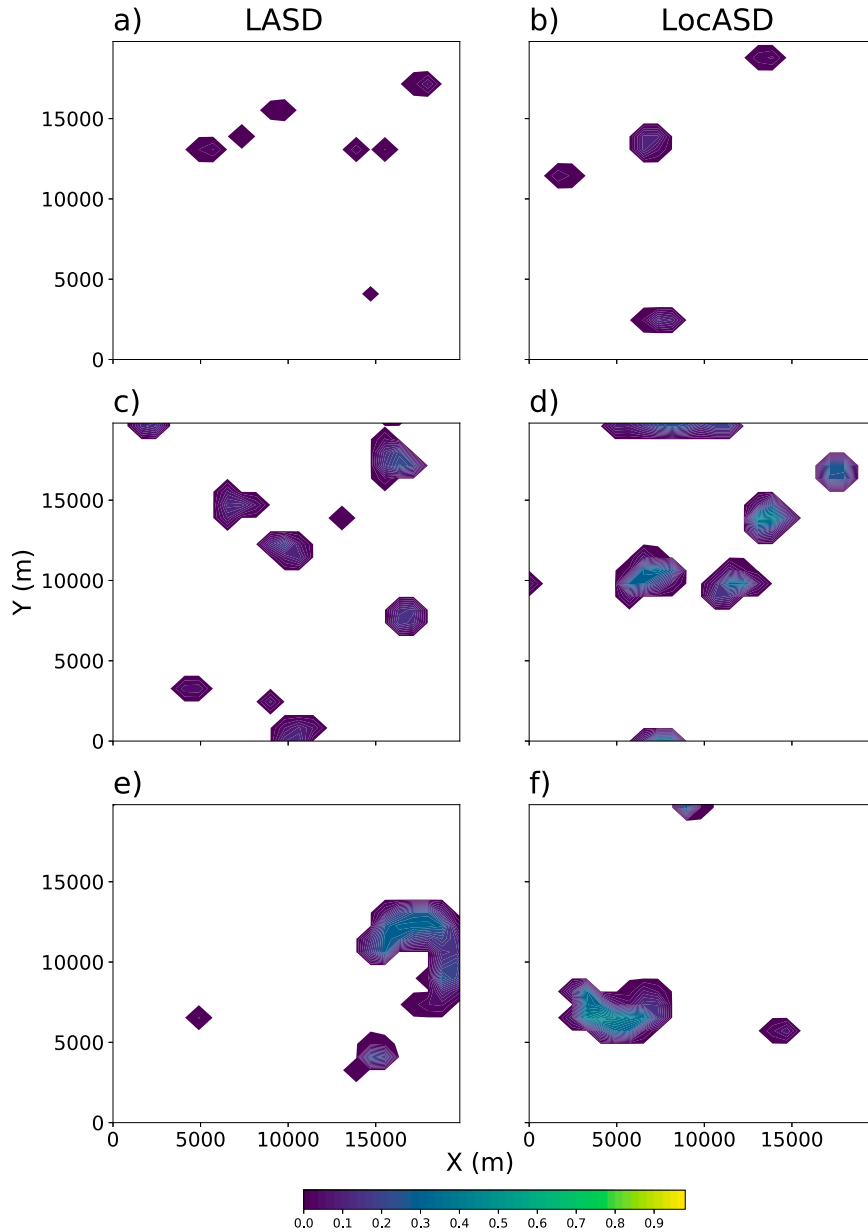


FIG. 14. Horizontal cross section of \bar{q}_l (g kg^{-1}) at height of maximum cloud cover for the $\Delta x = 800$ m run for the (a) ONSET LASD, (b) ONSET LocASD, (c) DEV LASD, (d) DEV LocASD, (e) QSS LASD, and (f) QSS LocASD runs. A part of the domain is shown to correspond to the same domain size as in the LES run. The plots only show grid points where $\bar{q}_l \geq 10^{-6} \text{ g g}^{-1}$.

Dynamic eddy-diffusivity schemes have been shown to suppress SGS mixing in the cloud layer where the potential temperature increases with height (Shi et al. 2018, 2019). This gives rise to more resolved heat transport (as in this case) or to countergradient fluxes when models that produce backscatter (such as mixed models) are used (Shi et al. 2018). As seen in Fig. 10 the filtered LES fluxes gradually become countergradient in the cloud layer (Figs. 10e,h) with heat flux increasing with height. Moreover, the inability of the local dynamic

Smagorinsky model to provide nonlocal fluxes underlines its usability limit when applied at resolutions too coarse to resolve any turbulent motions (see also Efsthathiou et al. 2018).

4) VERTICAL VELOCITY SPECTRA

The 2D vertical velocity spectra in the middle of the BL are presented in Fig. 11 for the 200, 400, and 800 m runs at DEV time. Spectra depict the impact of coarsening horizontal

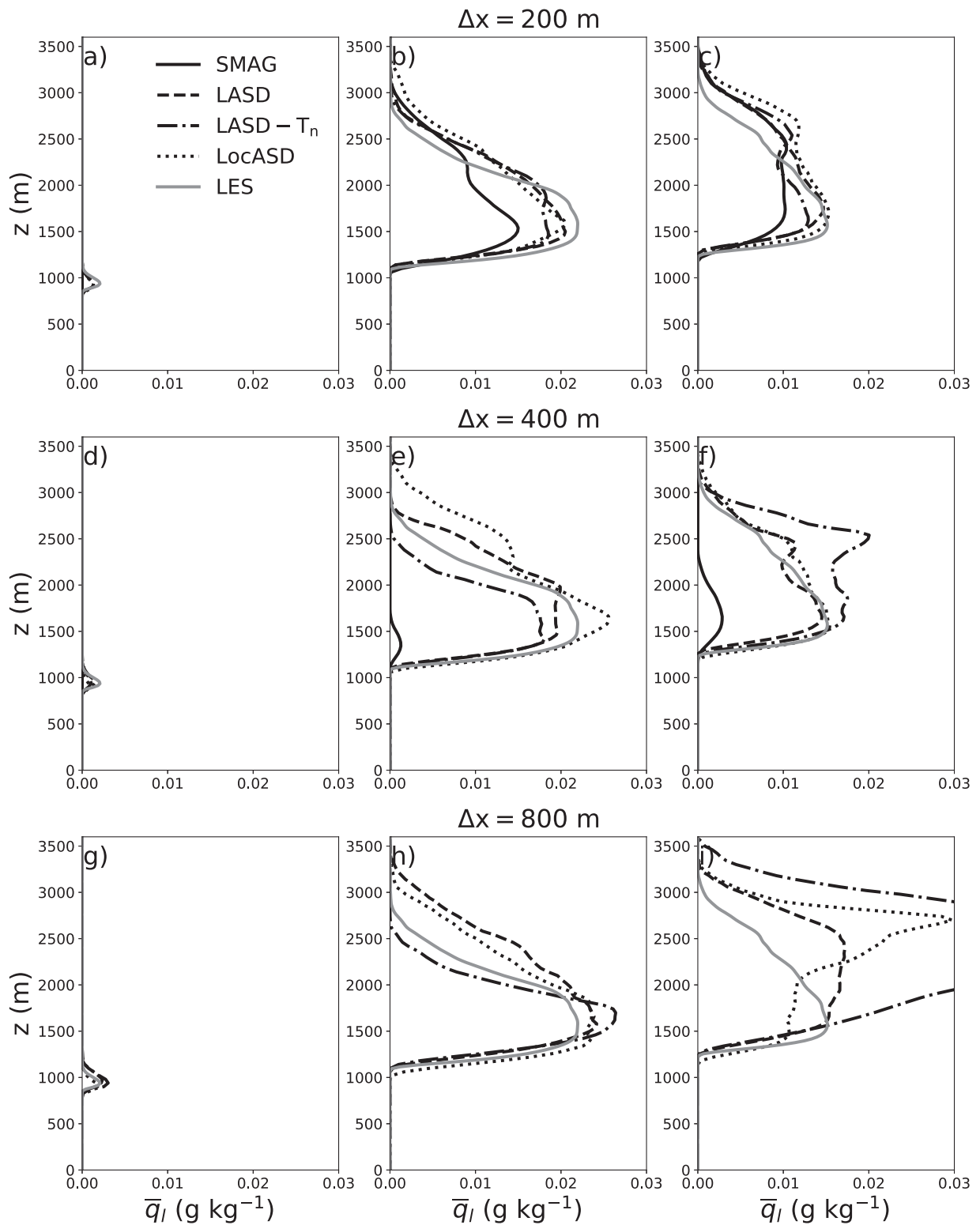


FIG. 15. Planar-averaged profiles of liquid water mixing ratio (\bar{q}_l ; g kg^{-1}) from the LES, SMAG, LASD, and LocASD simulations using different horizontal grid resolutions, specified at four different stages during the simulation: (a) 200 m ONSET, (b) 200 m DEV, (c) 200 m QSS, (d) 400 m ONSET, (e) 400 m DEV, (f) 400 m QSS, (g) 800 m ONSET, (h) 800 m DEV, and (i) 800 m QSS. Note that for the 800 m SMAG run, there are no profiles for (g)–(i) as the simulation crashed.

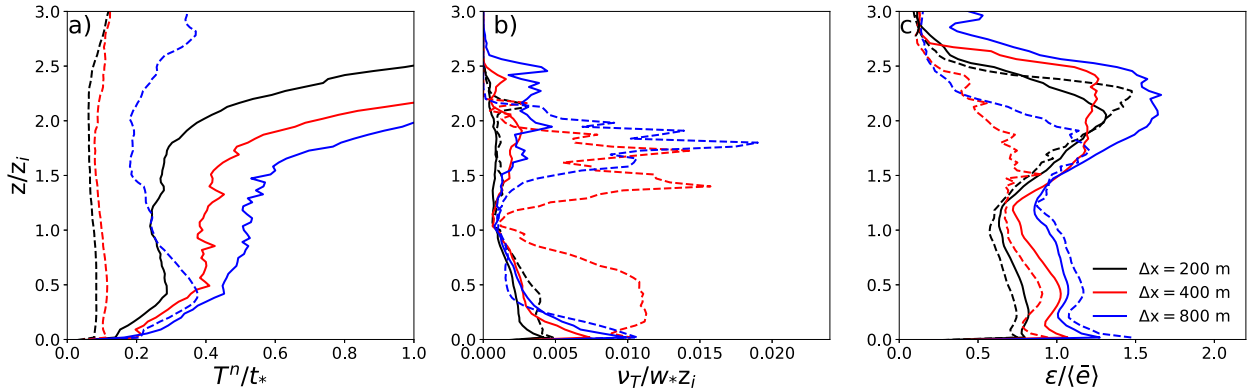


FIG. 16. Planar-averaged profiles of the (a) Lagrangian time scale normalized by the BL eddy turnover time ($t_* = z_i/w_*$), (b) normalized turbulent viscosity, and (c) Germano-identity error (ϵ) normalized by the planar-averaged profile of resolved TKE ($\langle \bar{\epsilon} \rangle$) from the $\Delta x = 200, 400,$ and 800 m LASD (solid lines) and LASD-Tn (dashed lines) simulations at DEV stage.

resolution on the resolved field as dissipation starts to affect the dominant scales of turbulence production (see Beare 2014). The diffusive nature of the standard Smagorinsky scheme results in strong damping of resolved motions that is exhibited by the fairly short inertial subrange at 200 m, which becomes almost nonexistent at 400 m. The dynamic models maintain a resolved inertial subrange for higher wavenumbers compared to SMAG with LASD being the most energetic, exhibiting less dissipation near the grid scale (see also Fig. 7).

At 200 m (Fig. 11a) all runs reproduce the dominant turbulence production at the right scales (as shown by the black dashed line that represents the LES spectra peak). However, at 400 m SMAG shift its peak at larger scales compared to the LES. Even though the spectra are calculated from a single time snapshot, this is a consistent behavior across different times during the DEV stage (not shown). The misrepresentation of the BL structure at 400 m SMAG run, as also seen in the mean and fluxes profiles (Figs. 5–10), contributes to the inability of SMAG to capture the cloud evolution and development.

The 800 m grid cannot resolve thermals on their natural scales; therefore, there is a shift to much larger scales as seen in Fig. 11c. In fact, the dominant LES production scales are found close to the Nyquist limit for the 800 m simulation. LASD produces a peak toward smaller BL structures and clearly exhibits lack of small-scale dissipation, substantially compromising the numerical solution due to numerical errors. Nonetheless, LocASD has a smoother maximum which is shifted to lower wavenumbers (larger scales) while there is stronger dissipation near the grid scale. This is reflected by the closer agreement of LocASD turbulence intensity with the filtered LES fields at $\Delta x = 800$ m compared to the LASD simulation (Figs. 7k,l).

5) CLOUD WATER CROSS SECTIONS

Figures 12–14 show a horizontal cross section of liquid water mixing ratio for the 200, 400, and 800 m runs, respectively, at $z = 880$ m (ONSET stage), 1200 m (DEV stage), and

1400 m (QSS stage) which are heights close to the cloud base. Figure 12 also contains the corresponding LES output for comparison. Clouds start to appear during the ONSET stage except in SMAG simulations which completely miss the formation of early clouds on the 200 and 400 m simulations. The evolution of cloud development in all simulations follows the LES in terms of their relative scale; increasing their size from the ONSET to the DEV stages as turbulence length scales become broader. However, their size also increases with coarsening resolutions leading to much bigger and fewer clouds seen at the 800 m LASD and LocASD runs. Note that the SMAG simulation crashed around the middle of the simulation before any condensation occurred.

At $\Delta x = 200$ m (Fig. 12) only small differences exist among the LASD, LocASD, SMAG, and the LES runs. However, SMAG produces smaller cloud cover compared to both dynamic runs as also verified by examining the cloud fraction especially at the lower cloud layer (not shown). Moreover, some larger clouds can be observed at the DEV stage (Fig. 12e) that can be related to the delayed SMAG spinup. Nevertheless, the biggest differences between the dynamic and SMAG runs emerge at $\Delta x = 400$ m (Fig. 13) where SMAG exhibits particularly poor cloud representation, producing significantly less clouds (almost half the LES cloud cover) compared to LASD and LocASD which almost have the same cloud cover as the LES (see also Fig. 4c). Only LASD and LocASD runs produce clouds at 800 m (Fig. 14) with LASD exhibiting more gridscale structures while LocASD seems to produce slightly more diffused and larger clouds in accordance with the vertical velocity spectra plot (Fig. 11c).

The findings from cloud water cross sections are further supported by Fig. 15 which shows the mean liquid water mixing ratio during the same times. SMAG produces less cloud water compared to the dynamic runs and the LES in average even from the 200 m run, becoming much more pronounced in the 400 m runs where SMAG cloud water is minimal. LASD and LocASD roughly follow the LES with LocASD showing slightly overshooting cloud especially at the 400 and 800 m simulations (Figs. 15e,h,i).

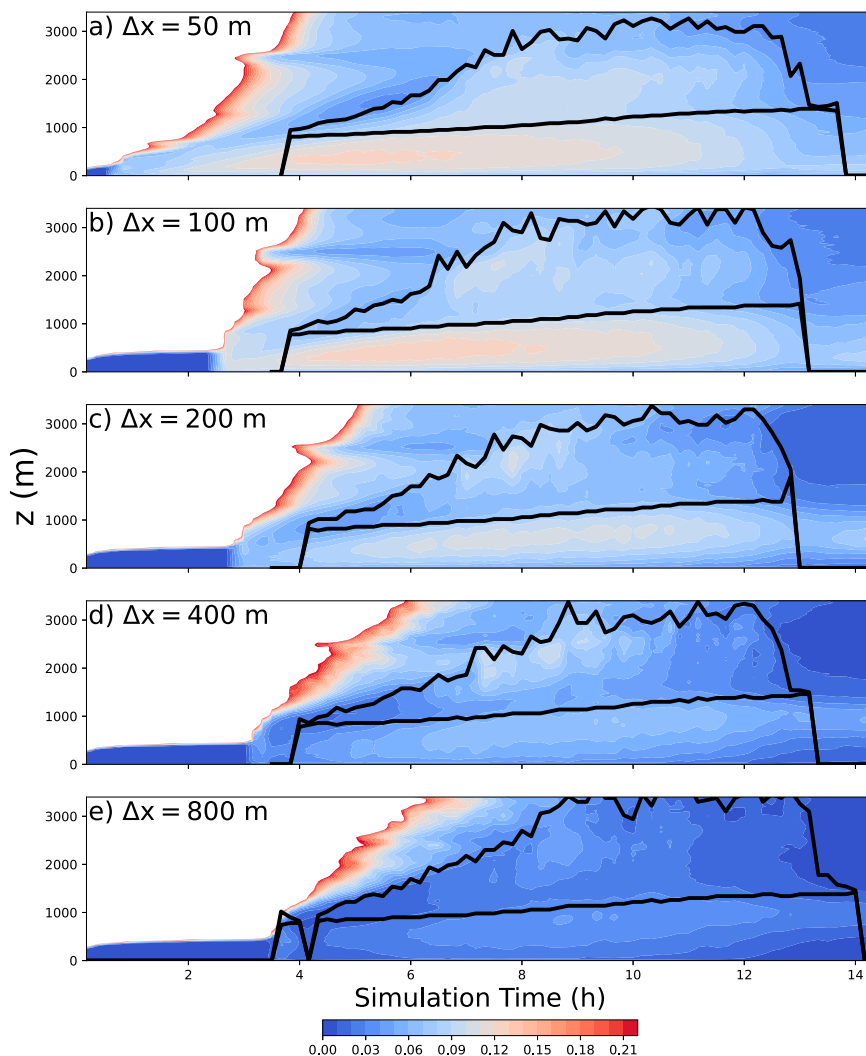


FIG. 17. Time evolution of planar-averaged C_S profiles from LASD simulations using different horizontal grid resolutions (Δx) (a) 50, (b) 100, (c) 200, (d) 400, and (e) 800 m. White denotes values outside the specified C_S range while black lines represent the cloud-base and cloud-top height evolution.

c. Impact of Lagrangian time scale

The Lagrangian time scale controls the memory of the averaging procedure according to Eqs. (41) and (42) through the adjustable parameter ϕ . The existence of a tunable parameter could limit the universal applicability of the dynamic approach. Research in the engineering community has shown significant sensitivity of complex flows to the choice of ϕ (Verma and Mahesh 2012). Additionally, Park and Mahesh (2009) showed that the corresponding Lagrangian correlation time scale does not significantly differentiate between the solid boundary and the interior of the flow. Therefore, the strong dependence of T^n in Eq. (41) on the strain rate through M_{ij} leads to a substantial mismatch with the diagnosed autocorrelation time scale (Park and Mahesh 2009).

To overcome the limitations emerging from the ad hoc specification of T^n , VerHulst and Meneveau (2012) suggested

a new dynamic time scale for LASD based on the error of the Germano identity due to the C_S approximation. The new time scale follows the dynamic method of Park and Mahesh (2009) which derives a surrogate autocorrelation time scale by reducing the Germano-identity error along flow pathlines. VerHulst and Meneveau (2012) directly related the time scale to the error utilizing a formulation proportional to the Taylor microscale of turbulent processes:

$$T^n = \pi \left\{ \frac{\langle (e_{ij} e_{ij})^2 \rangle}{\left[\left| \frac{d(e_{ij} e_{ij})}{dt} \right| \right]^2} \right\}^{1/2}. \quad (44)$$

Here we make a tentative initial exploration of one alternative, adopting Eq. (44) and test the new time scale at $\Delta x = 200, 400,$ and 800 m. The current implementation uses

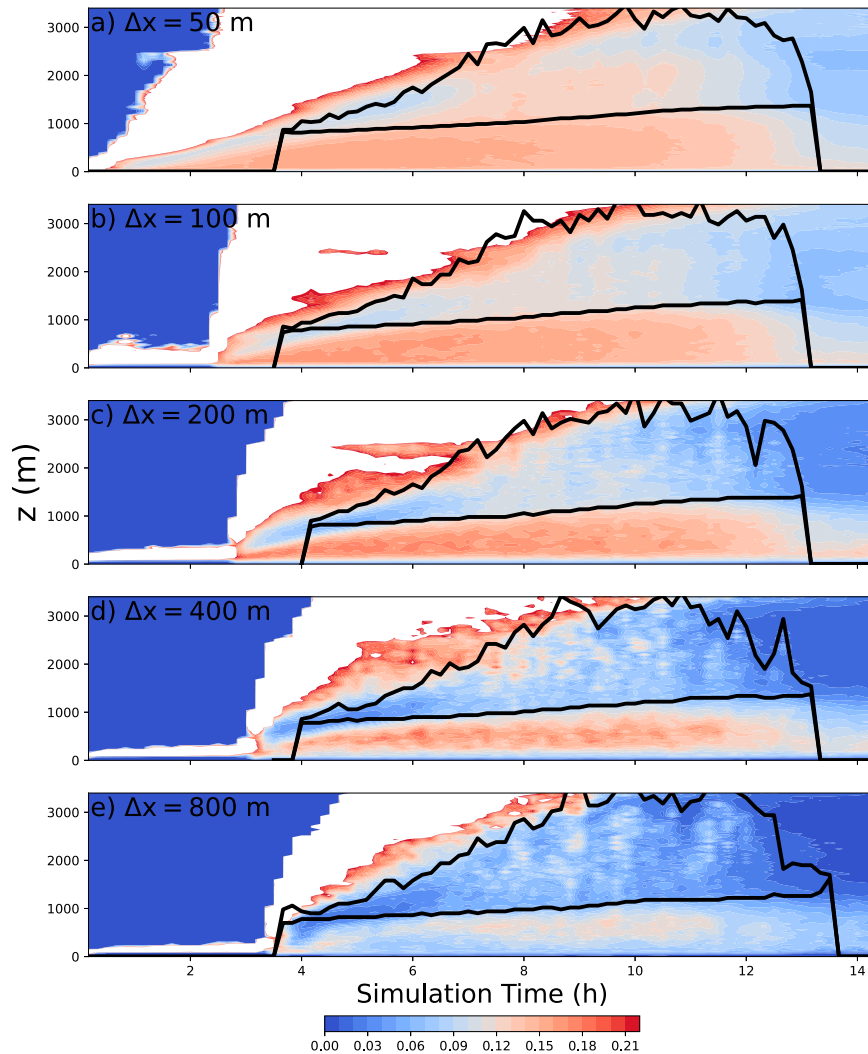


FIG. 18. As in Fig. 17, but for the LocASD simulations.

the same time scale for both momentum and scalar fluxes as well as the two filtering scales, substituting both Eqs. (41) and (42) with Eq. (44). A detailed evaluation of the new time scale is beyond the scope of this study. The error of the Germano identity is given by Eq. (17); however, it is calculated by using the final C_S from Eq. (25). The nominator and denominator are also averaged along pathlines according to Eq. (38), with the material derivative approximated by a first-order upwind scheme (see also VerHulst and Meneveau 2012).

The use of the new time scale (LASD-Tn) produces almost indistinguishable first-order quantities (potential temperature and water vapor mixing ratio) to the standard LASD and therefore not plotted in Figs. 5 and 6. The planar- and time-averaged resolved velocity variance in Fig. 7 depicts considerably less turbulence intensity at 200 and 400 m simulations when the new time scale is used. The above is evident in the 2D vertical velocity spectra (Figs. 11a,b) where LASD-Tn exhibits stronger dissipation. Some differences are present between

LASD and LASD-Tn especially at 400 m, where LASD-Tn is producing some stronger resolved fluxes during the DRY stage (see Figs. 7e, 8e, and 9d). Nonetheless, at 800 m LASD-Tn clearly displays lack of adequate dissipation, even worse compared to LASD (see Figs. 7k,l), with a pronounced accumulation of energy at small scales (Fig. 11c). The more energetic resolved flow has a notable impact on the heat fluxes during the DRY stages, resulting in stronger entrainment fluxes compared to LES (see Figs. 9g,i). Overenergetic structures also affect the total water transport especially at QSS stage (Fig. 8l) and the liquid water vertical profiles subsequently as can be seen in Fig. 15i.

The new dynamic time-scale formulation considerably reduces the planar-averaged Lagrangian time scale compared to the Meneveau et al. (1996) formula at the 200 and 400 m runs as shown in Fig. 16a (see also Park and Mahesh 2009), where the DEV stage is chosen as an example. Shorter (more local) averaging leads to increased turbulent viscosity (Fig. 16b) that in turn results in decreasing turbulence intensity, closely

following LocASD and the filtered fields compared to LASD (see Fig. 7). Furthermore, the new formulation produces a smaller Germano-identity error compared to LASD especially near the surface (Fig. 16c) where dynamic schemes are more prone to numerical errors. Overall, even though turbulent structures are less energetic that does not result in significant differences in the turbulent transports among the dynamic runs. At 800 m the behavior is reversed with LASD-Tn and LASD producing very similar time scales that are comparable to the BL eddy turnover time (Fig. 16a). Eddy-viscosity values in the lowest half of the BL become almost identical which results in much larger errors, especially for LASD-Tn. The increased Germano-identity error at 800 m reveals the limitations of the dynamic approach at such coarse resolutions mainly near the surface, where turbulent eddies become insufficiently resolved for the 800 m grid.

4. Length-scale evolution

Figures 17 and 18 depict the time evolution of the planar-averaged C_S [which can be related to the subgrid length scales through Eq. (7)] from all LASD and LocASD runs, respectively. A notable difference between LASD and LocASD is the higher C_S values seen in the LocASD simulations even from the 50 m run (see Fig. 18a), explaining the stronger dissipation seen in Fig. 7. Stoll and Porté-Agel (2008) also derived substantially larger C_S when local averaging was used instead of the Lagrangian approach. Nonetheless, both LASD and LocASD exhibit strong dependence on the BL stability, with C_S values increasing as the BL evolves, reaching a maximum at about 8 h after the start of the simulation (that roughly corresponds to the timing of maximum heat flux) and then decreasing afterward. In LASD, C_S tends to zero in the early stable BL regime (see Fig. 17a), while small values are maintained for longer until resolved motion spins up at lower resolutions (Figs. 17b–e). The same is true for the LocASD simulations; nevertheless, absolute C_S values are larger in comparison to LASD. Another notable difference is the significant clipping of negative values occurring in LocASD, about 30%–35% at all resolution runs [similar values have been reported by Basu and Porté-Agel (2006) and Stoll and Porté-Agel (2008)] while in LASD this varies to about 10%–15%.

Moreover, the dynamic SGS turbulence length scale captures the stability changes that occur as a function of height within the BL, with the length scale increasing away from the surface and decreasing close to the statically stable inversion. In LASD there is a clear dependence of C_S on horizontal resolution; the same diurnal evolution is evident across the different Δx runs while maximum C_S values become smaller. In contrast, LocASD maintains an almost constant maximum C_S before its values are substantially reduced in the 800 m run (Fig. 18e).

To demonstrate the stability and resolution dependence of LASD, Fig. 19 shows the mixing length (λ) values from all LASD runs at the first grid point above the surface layer as a function of Δ/L_{loc} where L_{loc} is local Monin–Obukhov length calculated as in Kumar et al. (2006). The use of L_{loc} aims to

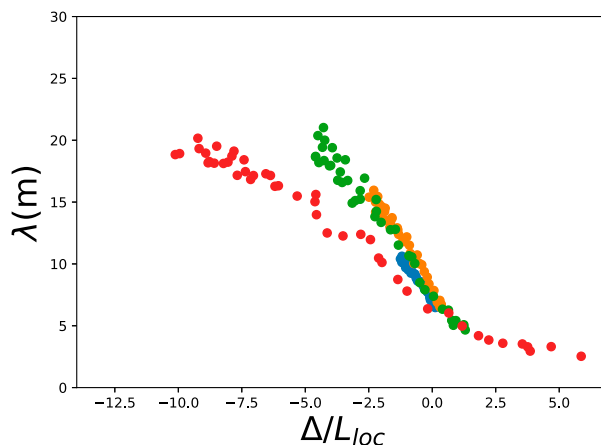


FIG. 19. Values of mixing length (λ) at the first grid point above the surface layer as a function of grid spacing ($\Delta = \Delta x$) normalized by the local Monin–Obukhov length (L_{loc}) from the LASD run. Corresponding values are sampled every 600 s, from 6 h after the start to the simulation end. Different filled circles represent data from the $\Delta x = 100$ m (blue), 200 m (orange), 400 m (green), and 800 m (red) runs.

avoid the hysteresis effect between λ and other parameters such as the standard Monin–Obukhov length due to its different behavior during the morning and evening transitions (see Kumar et al. 2006). However, some of the hysteresis was present in the 800 m LASD run; therefore, the sampling of the values shown in Fig. 19 begins at about 6 h after the start of the simulation. The mixing length seems to collapse fairly well against Δ/L_{loc} except the 800 m run that exhibits a slightly different behavior in unstable conditions. Two asymptotic limits can be identified; λ achieves its maximum values in the unstable/lower-resolution regime while asymptotically reducing to zero as stability increases. This behavior is similar to the empirical profile derived from the HATS dataset (Kleissl et al. 2004).

In the cloud layer, the planar-averaged C_S values are significantly lower compared to the BL as mostly represent the non-cloudy stable environment. Figures 20 and 21 display the conditionally averaged C_S at cloudy grid points. It becomes obvious that C_S is much larger inside clouds as these are highly turbulent structures with very strong vertical velocities (much larger than corresponding BL maximum w). Maximum C_S values are observed in the mid–upper part of the clouds mainly due to the stronger w found at those heights and also due to the sampling of much less clouds especially at lower resolutions. The same pattern as in the unconditionally averaged C_S is obvious with LocASD producing higher and less smooth values in the cloud layer, mostly at lower resolutions (Figs. 21c–e).

The Prandtl number remains relatively unchanged in the BL at all resolutions for both LASD and LocASD simulations varying from 0.5 to 0.7 in the middle of the BL (not shown). This means that C_S and C_θ change similarly across the scales and stability regimes. One notable difference is the increase of Pr near the surface as resolution coarsens (see also Li 2016).

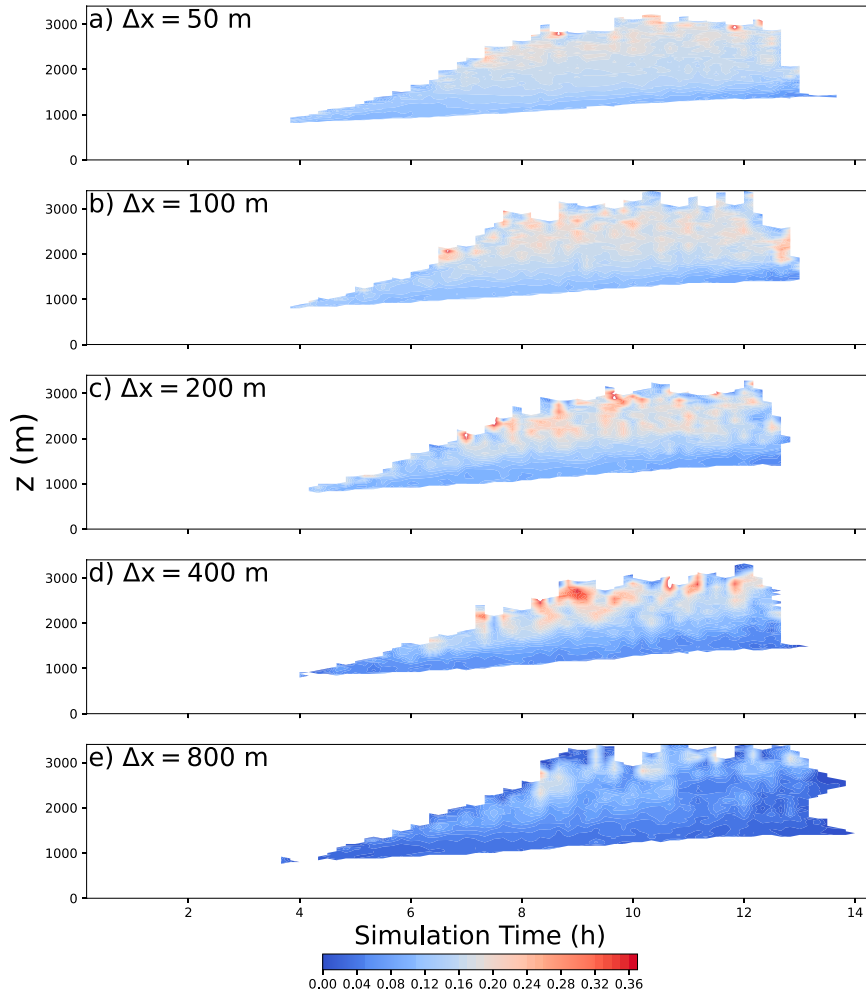


FIG. 20. As in Fig. 17, but for C_5 conditionally averaged in grid points where $\bar{q}_l \geq 10^{-6} \text{ g g}^{-1}$.

In the cloud layer, as mentioned, Pr increases significantly as C_θ becomes smaller especially at coarser resolutions.

5. Discussion and concluding remarks

The ARM case study offers a valuable test bed for exploring the impact of SGS turbulence closures in nonsteady state conditions of BL and shallow cumulus development. As the turbulence length scales evolve during the diurnal cycle, the simulation transitions from the gray zone to the LES and vice versa or enters multiple gray-zone regimes depending on Δ/Λ . An SGS length scale that does not adapt to the changes of the resolved turbulent field in time, space, and Δ not only appears unphysical but also has a detrimental effect on the representation of the BL and cloud structures even from relatively fine resolutions, as shown in this study.

LES closures, such as the standard Smagorinsky scheme, have been preferred for subkilometric to kilometric cloud-resolving simulations, especially for deep convection modeling, over 1D RANS schemes (Parodi and Tanelli 2010; Fiori et al. 2010; Machado and Chaboureau 2015). Nonetheless,

subkilometric simulations are eventually found in the gray zone and even though the 3D nature of LES diffusion approaches seems beneficial for the scales of deep clouds, severe shortcomings in the representation of BL and shallow clouds have been observed (Shi et al. 2019). The overdiffusive nature of Smagorinsky becomes obvious from relatively fine resolutions in the simulation of the ARM case. The most striking feature of SMAG runs is the late spinup of resolved motion that leads to the significant delay of cloud development. The lack of overturning motion results in moisture being confined in the BL, which in turn appears cooler and more humid with early superadiabatic potential temperature profiles, compared to the reference LES. On top of that, strong downgradient diffusion of scalars in the cloud layer controls the total water and heat transport through the fixed values of C_5 and mainly Pr. At $\Delta x = 200 \text{ m}$ SMAG completely misses the ONSET and misrepresents a substantial part of the DEV stage before cumulus clouds become fully established. Furthermore, the inaccurate BL and cloud layer representation becomes much worse at 400 m significantly limiting its ability to reproduce any stage of cloud evolution. At

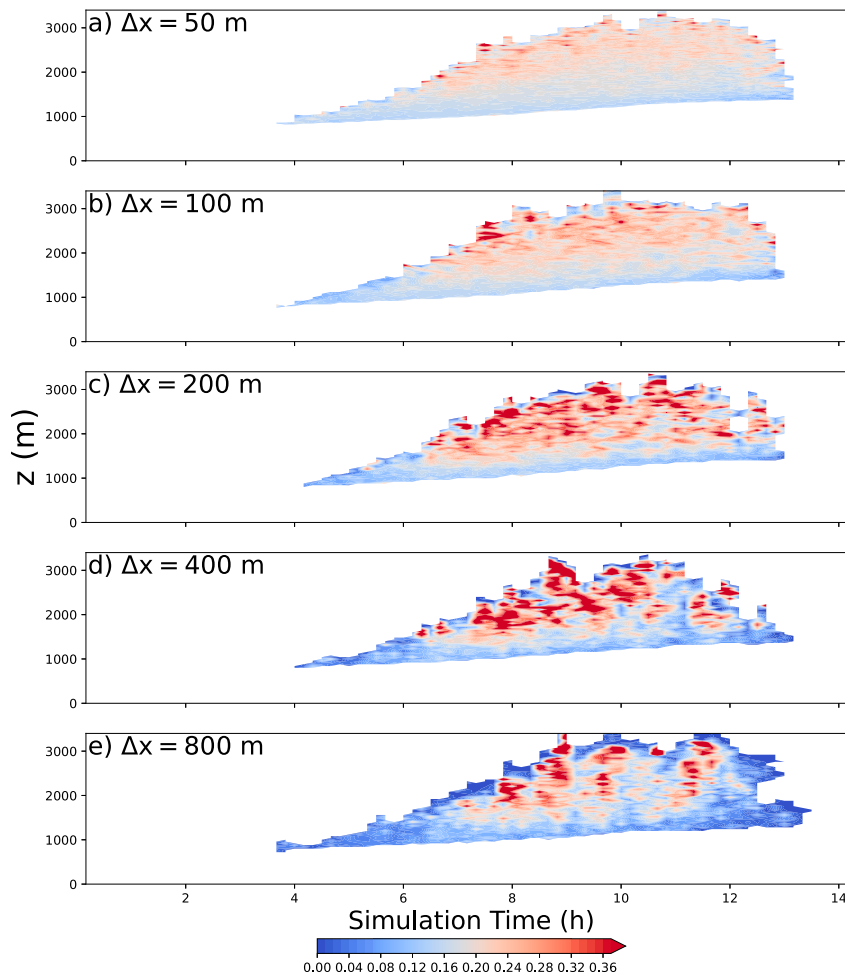


FIG. 21. As in Fig. 20, but for LocASD.

800 m, SMAG fails to produce any condensation as the run crashes midway.

Introducing the scale-dependent, Lagrangian-averaged dynamic Smagorinsky model (Bou-Zeid et al. 2005; Efstathiou et al. 2018) to simulate the ARM case study at gray-zone resolutions leads to a significant improvement of the BL representation and subsequent cloud development compared to SMAG. Similar to the findings of Efstathiou et al. (2018) for a dry CBL case, LASD runs exhibit faster spinup of resolved motion, reproducing the reference LES first-order profiles and total water transport across the scales. As a result, cloud onset, development, and dissipation occur at roughly the same time in all runs. However, LASD produces more energetic turbulence structures compared to the coarse-grained reference LES fields, especially during the DEV and QSS stages, that has a slight impact on the BL temperature and moisture profiles. A local averaging version of LASD (LocASD) was also introduced which was able to better follow the coarse-grained LES fields but does not scale particularly well with grid resolution. Mixing-length values become considerably higher and less smooth in space compared to

LASD, leading to reduced turbulence intensity in the BL. Nevertheless, differences between LASD and LocASD profiles and cloud properties are much smaller in relation to the corresponding dynamic schemes—SMAG differences and the SMAG–LES discrepancies.

The turbulence intensity in the BL can be related to the choice of the averaging time scale for LASD. The conventional time scale depends strongly on the strain rate. As shear production is substantial in the ARM case compared to low-shear CBLs (see Efstathiou et al. 2018), the time scale is considerably increased (mainly near the surface) leading to less local sampling and smaller C_S values in this case. By tentatively adopting a new formulation for the dynamic Lagrangian time scale, based on the error of the Germano identity (see VerHulst and Meneveau 2012), the Lagrangian time scale complies with the findings of Park and Mahesh (2009). Hence, the time scale becomes more local producing larger C_S values. In any case, more work is needed before the potential benefits of the new, dynamic Lagrangian time scale can be fully established.

Despite its incorporated scale awareness through Eq. (7) and stability dependence through the stability functions,

SMAG is not able to reproduce the turbulence scale evolution as it requires Δ to lie in the inertial subrange; a condition which is violated outside the LES regime i.e., when the BL is shallow or grid resolution is coarse. A scale-, space-, and time-dependent mixing-length formulation seems capable of extending LES closures to the near-gray-zone or gray-zone regime depending on Δ/Λ . The dynamic Smagorinsky exhibits excellent transition properties across stability regimes as it relaxes the fundamental assumptions behind the standard Smagorinsky scheme. On the other hand, a local eddy-diffusivity formulation is inherently unable to produce countergradient fluxes as can be seen in Fig. 10. In fact, both dynamic approaches seem to significantly reduce the local turbulent transport in clouds by reducing C_θ (increasing Pr). This is a limitation for the use of the dynamic Smagorinsky farther into the gray zone where flow is only marginally resolved. Moreover, the errors related to the Germano identity when the turbulence field is very poorly resolved, as shown at the 800 m LASD run, underlines a practical usability limit for the dynamic approach (see also Efstathiou et al. 2018).

Overall, the dynamic approach provides significant improvements in the representation of BL driven shallow convection at gray-zone resolutions due to its ability to represent transitions and its strong scale dependency. The overdiffusive nature of the conventional Smagorinsky scheme results in the significantly delayed spinup of resolved motion and misrepresentation of cloud development. However, it should be noted that the dynamic approach solely relies on resolved motion to represent nonlocal turbulent transports. Furthermore, LASD seems to become overenergetic when the BL is fully developed. Nonetheless, local averaging (LocASD) or removing the dependency of the averaging time scale on shear, can provide more dissipation without compromising the results. These approaches seem to overcome the aforementioned issues, with the LocASD being more attractive for NWP applications due to its simplicity. The recent trend of increasing the horizontal resolution of regional NWP from the kilometeric to the subkilometric regime makes dynamic turbulence modeling increasingly relevant in operational settings as weather centers like the Met Office are already experimenting with their 333 m configuration of the UM model (Boutle et al. 2016). In any case, dynamic mixed schemes can account for nonlocal fluxes through explicitly utilizing the extra Leonard terms (see Shi et al. 2019). Future work will focus on examining different dynamic approaches and identifying possible benefits in gray-zone deep convection simulations.

Acknowledgments. This work was supported by the UKRI Natural Environment Research Council (Grant NE/T011351/1). For the purpose of open access, the author has applied a Creative Commons Attribution (CC BY) license to any author accepted manuscript version arising. We acknowledge use of the Monsoon2 system, a collaborative facility supplied under the Joint Weather and Climate Research Programme, a strategic partnership between the Met Office and the Natural Environment Research Council.

Data availability statement. The LES performed in this study will be available from the University of Exeter’s institutional repository at <https://doi.org/10.24378/exe.4604> following a 2-yr embargo.

APPENDIX

Stability Functions

Following Efstathiou et al. (2018), the stability functions (Brown et al. 1994) are included in the implementation of LASD and LocASD in a consistent way where they are part of the filtering process during the dynamic procedure (see also Kirkpatrick et al. 2006). Bopape et al. (2021) concluded that the use of stability functions improves the behavior of the LASD model especially in the gray-zone regime. The benefit from using the stability correction is expected to be more pronounced near the surface where the flow is strongly unstable and at coarser resolutions where the dynamic model samples from underresolved scales, which are prone to truncation errors.

The stability functions depend on the moist Richardson number in the presence of moisture, which is calculated based on the change in subgrid buoyancy flux when a fraction of potential energy is exchanged between two layers during parcel ascent and mixing, following MacVean and Mason (1990). The moist Richardson number is computed at the grid scale and the two different test scales as a function of the filtered strain rate, temperature, vapor, and liquid water fields $(\bar{S}_{ij}, \bar{\theta}, \bar{q}_v, \bar{q}_l)$. More specifically, at the scale of the 2Δ filter it is $\bar{Ri} = Ri(\bar{S}_{ij}, \bar{\theta}, \bar{q}_v, \bar{q}_l)$ while at scales 4Δ it is $\hat{Ri} = Ri(\hat{S}_{ij}, \hat{\theta}, \hat{q}_v, \hat{q}_l)$. After Ri is determined, the stability functions are calculated using the functional forms of Brown et al. (1994). For statically unstable conditions ($Ri < 0$),

$$f_m(Ri) = (1 - 16Ri)^{0.5}, \tag{A1}$$

$$f_h(Ri) = (1 - 40Ri)^{0.5}, \tag{A2}$$

and for the statically stable regime ($0 \leq Ri < 0.25$),

$$f_m(Ri) = \left(1 - \frac{Ri}{0.25}\right)^4, \tag{A3}$$

$$f_h(Ri) = \left(1 - \frac{Ri}{0.25}\right)^4 (1 - 1.2Ri), \tag{A4}$$

while f_m and f_h are set to zero in the dynamically stable regime ($Ri \geq 0.25$). Note that Pr is usually included in the stability functions formulations; in this implementation the Pr is included in Eqs. (9) and (10) and inferred through the dynamic calculation of C_θ in the dynamic model [Eq. (28)].

REFERENCES

Basu, S., and F. Porté-Agel, 2006: Large-eddy simulation of stably stratified atmospheric boundary layer turbulence: A scale-dependent dynamic modeling approach. *J. Atmos. Sci.*, **63**, 2074–2091, <https://doi.org/10.1175/JAS3734.1>.

- , J.-F. Vinuesa, and A. Swift, 2008: Dynamic LES modeling of a diurnal cycle. *J. Appl. Meteor. Climatol.*, **47**, 1156–1174, <https://doi.org/10.1175/2007JAMC1677.1>.
- Bauer, P., A. Thorpe, and G. Brunet, 2015: The quiet revolution of numerical weather prediction. *Nature*, **525**, 47–55, <https://doi.org/10.1038/nature14956>.
- Beare, R. J., 2014: A length scale defining partially-resolved boundary-layer turbulence simulations. *Bound.-Layer Meteor.*, **151**, 39–55, <https://doi.org/10.1007/s10546-013-9881-3>.
- Bolin, B., 1955: Numerical forecasting with the barotropic model. *Tellus*, **7**, 27–49, <https://doi.org/10.3402/tellusa.v7i1.8770>.
- Bopape, M.-J. M., R. S. Plant, O. Coceal, G. A. Efstathiou, and M. Valdivieso, 2021: Effects of stability functions in a dynamic model convective boundary layer simulation. *Atmos. Sci. Lett.*, **22**, e1008, <https://doi.org/10.1002/asl.1008>.
- Bou-Zeid, E., C. Meneveau, and M. Parlange, 2005: A scale-dependent Lagrangian dynamic model for large eddy simulation of complex turbulent flows. *Phys. Fluids*, **17**, 025105, <https://doi.org/10.1063/1.1839152>.
- Boutle, I. A., J. E. J. Eyre, and A. P. Lock, 2014: Seamless stratocumulus simulation across the turbulent gray zone. *Mon. Wea. Rev.*, **142**, 1655–1668, <https://doi.org/10.1175/MWR-D-13-00229.1>.
- , A. Finnenkoetter, A. P. Lock, and H. Wells, 2016: The London Model: Forecasting fog at 333 m resolution. *Quart. J. Roy. Meteor. Soc.*, **142**, 360–371, <https://doi.org/10.1002/qj.2656>.
- Brown, A. R., S. H. Derbyshire, and P. J. Mason, 1994: Large-eddy simulation of stable atmospheric boundary layers with a revised stochastic subgrid model. *Quart. J. Roy. Meteor. Soc.*, **120**, 1485–1512, <https://doi.org/10.1002/qj.49712052004>.
- , and Coauthors, 2002: Large-eddy simulation of the diurnal cycle of shallow cumulus convection over land. *Quart. J. Roy. Meteor. Soc.*, **128**, 1075–1093, <https://doi.org/10.1256/003590002320373210>.
- Brown, N., A. Lepper, M. Weiland, A. Hill, B. Shipway, and C. Maynard, 2015: A directive based hybrid Met Office NERC Cloud model. *Proc. Second Workshop on Accelerator Programming Using Directives*, Austin, TX, Association for Computing Machinery, 7, <https://doi.org/10.1145/2832105.2832115>.
- Charney, J. G., R. Fjørtoft, and J. Von Neumann, 1950: Numerical integration of the barotropic vorticity equation. *Tellus*, **2**, 237–254, <https://doi.org/10.1111/j.2153-3490.1950.tb00336.x>.
- Chow, F. K., R. L. Street, M. Xue, and J. H. Ferziger, 2005: Explicit filtering and reconstruction turbulence modeling for large-eddy simulation of neutral boundary layer flow. *J. Atmos. Sci.*, **62**, 2058–2077, <https://doi.org/10.1175/JAS3456.1>.
- Efstathiou, G. A., and R. J. Beare, 2015: Quantifying and improving sub-grid diffusion in the boundary-layer grey zone. *Quart. J. Roy. Meteor. Soc.*, **141**, 3006–3017, <https://doi.org/10.1002/qj.2585>.
- , and R. S. Plant, 2019: A dynamic extension of the pragmatic blending scheme for scale-dependent sub-grid mixing. *Quart. J. Roy. Meteor. Soc.*, **145**, 884–892, <https://doi.org/10.1002/qj.3445>.
- , R. J. Beare, S. Osborne, and A. P. Lock, 2016: Grey zone simulations of the morning convective boundary layer development. *J. Geophys. Res. Atmos.*, **121**, 4769–4782, <https://doi.org/10.1002/2016JD024860>.
- , R. S. Plant, and M.-J. M. Bopape, 2018: Simulation of an evolving convective boundary layer using a scale-dependent dynamic Smagorinsky model at near-gray-zone resolutions. *J. Appl. Meteor. Climatol.*, **57**, 2197–2214, <https://doi.org/10.1175/JAMC-D-17-0318.1>.
- Fiori, E., A. Parodi, and F. Siccardi, 2010: Turbulence closure parameterization and grid spacing effects in simulated supercell storms. *J. Atmos. Sci.*, **67**, 3870–3890, <https://doi.org/10.1175/2010JAS3359.1>.
- Germano, M., U. Piomelli, P. Moin, and W. H. Cabot, 1991: A dynamic subgrid-scale eddy viscosity model. *Phys. Fluids*, **3A**, 1760–1765, <https://doi.org/10.1063/1.857955>.
- Hanley, K. E., R. S. Plant, T. H. M. Stein, R. J. Hogan, J. C. Nicol, H. W. Lean, C. Halliwell, and P. A. Clark, 2015: Mixing-length controls on high-resolution simulations of convective storms. *Quart. J. Roy. Meteor. Soc.*, **141**, 272–284, <https://doi.org/10.1002/qj.2356>.
- Honnert, R., V. Masson, and F. Couvreux, 2011: A diagnostic for evaluating the representation of turbulence in atmospheric models at the kilometric scale. *J. Atmos. Sci.*, **68**, 3112–3131, <https://doi.org/10.1175/JAS-D-11-061.1>.
- , and Coauthors, 2020: The atmospheric boundary layer and the “gray zone” of turbulence: A critical review. *J. Geophys. Res. Atmos.*, **125**, e2019JD030317, <https://doi.org/10.1029/2019JD030317>.
- Ito, J., H. Niino, M. Nakanishi, and C.-H. Moeng, 2015: An extension of the Mellor–Yamada model to the terra incognita zone for dry convective mixed layers in the free convection regime. *Bound.-Layer Meteor.*, **157**, 23–43, <https://doi.org/10.1007/s10546-015-0045-5>.
- , S. Hayashi, A. Hashimoto, H. Ohtake, F. Uno, H. Yoshimura, T. Kato, and Y. Yamada, 2017: Stalled improvement in a numerical weather prediction model as horizontal resolution increases to the sub-kilometer scale. *SOLA*, **13**, 151–156, <https://doi.org/10.2151/sola.2017-028>.
- Juliano, T. W., B. Kosović, P. A. Jiménez, M. Eghdami, S. E. Haupt, and A. Martilli, 2022: “Gray zone” simulations using a three-dimensional planetary boundary layer parameterization in the Weather Research and Forecasting Model. *Mon. Wea. Rev.*, **150**, 1585–1619, <https://doi.org/10.1175/MWR-D-21-0164.1>.
- Kirkil, G., J. Mirocha, E. Bou-Zeid, F. K. Chow, and B. Kosović, 2012: Implementation and evaluation of dynamic subfilter-scale stress models for large-eddy simulation using WRF. *Mon. Wea. Rev.*, **140**, 266–284, <https://doi.org/10.1175/MWR-D-11-00037.1>.
- Kirkpatrick, M. P., A. S. Ackerman, D. E. Stevens, and N. N. Mansour, 2006: On the application of the dynamic Smagorinsky model to large-eddy simulations of the cloud-topped atmospheric boundary layer. *J. Atmos. Sci.*, **63**, 526–546, <https://doi.org/10.1175/JAS3651.1>.
- Kleissl, J., M. B. Parlange, and C. Meneveau, 2004: Field experimental study of dynamic Smagorinsky models in the atmospheric surface layer. *J. Atmos. Sci.*, **61**, 2296–2307, [https://doi.org/10.1175/1520-0469\(2004\)061<2296:FESODS>2.0.CO;2](https://doi.org/10.1175/1520-0469(2004)061<2296:FESODS>2.0.CO;2).
- Kumar, V., J. Kleissl, C. Meneveau, and M. B. Parlange, 2006: Large-eddy simulation of a diurnal cycle of the atmospheric boundary layer: Atmospheric stability and scaling issues. *Water Resour. Res.*, **42**, W06D09, <https://doi.org/10.1029/2005WR004651>.
- Kurowski, M. J., and J. Teixeira, 2018: A scale-adaptive turbulent kinetic energy closure for the dry convective boundary layer. *J. Atmos. Sci.*, **75**, 675–690, <https://doi.org/10.1175/JAS-D-16-0296.1>.
- Lancz, D., B. Szintai, and R. Honnert, 2018: Modification of a parameterization of shallow convection in the grey zone using a mesoscale model. *Bound.-Layer Meteor.*, **169**, 483–503, <https://doi.org/10.1007/s10546-018-0375-1>.
- Leonard, A., 1975: Energy cascade in large-eddy simulations of turbulent fluid flows. *Advances in Geophysics*, Vol. 18, Elsevier, 237–248, [https://doi.org/10.1016/S0065-2687\(08\)60464-1](https://doi.org/10.1016/S0065-2687(08)60464-1).

- Leonard, B. P., M. K. MacVean, and A. P. Lock, 1993: Positivity-preserving numerical schemes for multidimensional advection. NASA Tech. Memo. 106055, 64 pp., <https://ntrs.nasa.gov/api/citations/19930017902/downloads/19930017902.pdf>.
- Li, D., 2016: Revisiting the subgrid-scale Prandtl number for large-eddy simulation. *J. Fluid Mech.*, **802**, R2, <https://doi.org/10.1017/jfm.2016.472>.
- Lilly, D. K., 1967: The representation of small-scale turbulence in numerical simulation experiments. *Proc. IBM Scientific Computing Symp. on Environmental Sciences*, Yorktown Heights, NY, IBM, 195–210.
- , 1992: A proposed modification of the Germano subgrid-scale closure method. *Phys. Fluids*, **4A**, 633–635, <https://doi.org/10.1063/1.858280>.
- Machado, L. A. T., and J.-P. Chaboureau, 2015: Effect of turbulence parameterization on assessment of cloud organization. *Mon. Wea. Rev.*, **143**, 3246–3262, <https://doi.org/10.1175/MWR-D-14-00393.1>.
- MacVean, M. K., and P. J. Mason, 1990: Cloud-top entrainment instability through small-scale mixing and its parameterization in numerical models. *J. Atmos. Sci.*, **47**, 1012–1030, [https://doi.org/10.1175/1520-0469\(1990\)047<1012:CTEITS>2.0.CO;2](https://doi.org/10.1175/1520-0469(1990)047<1012:CTEITS>2.0.CO;2).
- Mason, P. J., 1989: Large-eddy simulation of the convective atmospheric boundary layer. *J. Atmos. Sci.*, **46**, 1492–1516, [https://doi.org/10.1175/1520-0469\(1989\)046<1492:LESOTC>2.0.CO;2](https://doi.org/10.1175/1520-0469(1989)046<1492:LESOTC>2.0.CO;2).
- , and D. J. Thomson, 1992: Stochastic backscatter in large-eddy simulations of boundary layers. *J. Fluid Mech.*, **242**, 51–78, <https://doi.org/10.1017/S0022112092002271>.
- Meneveau, C., T. S. Lund, and W. H. Cabot, 1996: A Lagrangian dynamic subgrid-scale model of turbulence. *J. Fluid Mech.*, **319**, 353–385, <https://doi.org/10.1017/S0022112096007379>.
- Park, N., and K. Mahesh, 2009: Reduction of the Germano-identity error in the dynamic Smagorinsky model. *Phys. Fluids*, **21**, 065106, <https://doi.org/10.1063/1.3140033>.
- Parodi, A., and S. Tanelli, 2010: Influence of turbulence parameterizations on high-resolution numerical modeling of tropical convection observed during the TC4 field campaign. *J. Geophys. Res.*, **115**, D00J14, <https://doi.org/10.1029/2009JD013302>.
- Petch, J. C., A. R. Brown, and M. E. B. Gray, 2002: The impact of horizontal resolution on the simulations of convective development over land. *Quart. J. Roy. Meteor. Soc.*, **128**, 2031–2044, <https://doi.org/10.1256/003590002320603511>.
- Piacsek, S. A., and G. P. Williams, 1970: Conservation properties of convection difference schemes. *J. Comput. Phys.*, **6**, 392–405, [https://doi.org/10.1016/0021-9991\(70\)90038-0](https://doi.org/10.1016/0021-9991(70)90038-0).
- Pope, S. B., 2000: *Turbulent Flows*. Cambridge University Press, 771 pp.
- Porté-Agel, F., C. Meneveau, and M. B. Parlange, 2000: A scale-dependent dynamic model for large-eddy simulation: Application to a neutral atmospheric boundary layer. *J. Fluid Mech.*, **415**, 261–284, <https://doi.org/10.1017/S0022112000008776>.
- Shi, X., H. L. Hagen, F. K. Chow, G. H. Bryan, and R. L. Street, 2018: Large-eddy simulation of the stratocumulus-capped boundary layer with explicit filtering and reconstruction turbulence modeling. *J. Atmos. Sci.*, **75**, 611–637, <https://doi.org/10.1175/JAS-D-17-0162.1>.
- , F. K. Chow, R. L. Street, and G. H. Bryan, 2019: Key elements of turbulence closures for simulating deep convection at kilometer-scale resolution. *J. Adv. Model. Earth Syst.*, **11**, 818–838, <https://doi.org/10.1029/2018MS001446>.
- Shin, H. H., and S.-Y. Hong, 2015: Representation of the subgrid-scale turbulent transport in convective boundary layers at gray-zone resolutions. *Mon. Wea. Rev.*, **143**, 250–271, <https://doi.org/10.1175/MWR-D-14-00116.1>.
- Simon, J. S., B. Zhou, J. D. Mirocha, and F. K. Chow, 2019: Explicit filtering and reconstruction to reduce grid dependence in convective boundary layer simulations using WRF-LES. *Mon. Wea. Rev.*, **147**, 1805–1821, <https://doi.org/10.1175/MWR-D-18-0205.1>.
- Smagorinsky, J., 1963: General circulation experiments with the primitive equations. *Mon. Wea. Rev.*, **91**, 99–164, [https://doi.org/10.1175/1520-0493\(1963\)091<0099:GCEWTP>2.3.CO;2](https://doi.org/10.1175/1520-0493(1963)091<0099:GCEWTP>2.3.CO;2).
- Stoll, R., and F. Porté-Agel, 2008: Large-eddy simulation of the stable atmospheric boundary layer using dynamic models with different averaging schemes. *Bound.-Layer Meteor.*, **126**, 1–28, <https://doi.org/10.1007/s10546-007-9207-4>.
- Sullivan, P. P., and E. G. Patton, 2011: The effect of mesh resolution on convective boundary layer statistics and structures generated by large-eddy simulation. *J. Atmos. Sci.*, **68**, 2395–2415, <https://doi.org/10.1175/JAS-D-10-05010.1>.
- VerHulst, C., and C. Meneveau, 2012: Dynamic time-scale for Lagrangian-averaged subgrid-scale models based on Rice’s formula. *Proc. 18th Australasian Fluid Mechanics Conf.*, Launceston, Australia, Australasian Fluid Mechanics Society, 956–959, <https://people.eng.unimelb.edu.au/imarusic/proceedings/18/403%20-%20Meneveau.pdf>.
- Verma, A., and K. Mahesh, 2012: A Lagrangian subgrid-scale model with dynamic estimation of Lagrangian time scale for large eddy simulation of complex flows. *Phys. Fluids*, **24**, 085101, <https://doi.org/10.1063/1.4737656>.
- Verrelle, A., D. Ricard, and C. Lac, 2015: Sensitivity of high-resolution idealized simulations of thunderstorms to horizontal resolution and turbulence parameterization. *Quart. J. Roy. Meteor. Soc.*, **141**, 433–448, <https://doi.org/10.1002/qj.2363>.
- Warren, R. A., D. J. Kirshbaum, R. S. Plant, and H. W. Lean, 2014: A ‘Boscastle-type’ quasi-stationary convective system over the UK southwest peninsula. *Quart. J. Roy. Meteor. Soc.*, **140**, 240–257, <https://doi.org/10.1002/qj.2124>.
- Wyngaard, J. C., 2004: Toward numerical modeling in the “terra incognita.” *J. Atmos. Sci.*, **61**, 1816–1826, [https://doi.org/10.1175/1520-0469\(2004\)061<1816:TNMITT>2.0.CO;2](https://doi.org/10.1175/1520-0469(2004)061<1816:TNMITT>2.0.CO;2).
- Zhang, X., J.-W. Bao, B. Chen, and E. D. Grell, 2018: A three-dimensional scale-adaptive turbulent kinetic energy scheme in the WRF-ARW Model. *Mon. Wea. Rev.*, **146**, 2023–2045, <https://doi.org/10.1175/MWR-D-17-0356.1>.
- Zhou, B., Y. Li, and S. Miao, 2021: A scale-adaptive turbulence model for the dry convective boundary layer. *J. Atmos. Sci.*, **78**, 1715–1733, <https://doi.org/10.1175/JAS-D-20-0240.1>.